# New Computational Methodologies for Microstructure Quantification

Richard K. Catania

Thesis submitted to the Faculty of the

Virginia Polytechnic Institute and State University

in partial fulfillment of the requirements for the degree of

Master of Science

in

Mechanical Engineering

Pinar Acar, Chair

Mehdi Ahmadian

Reza Mirzaeifar

April 21, 2022

Blacksburg, Virginia

# New Computational Methodologies for Microstructure Quantification

Richard K. Catania

(ABSTRACT)

This work explores physics-based and data-driven methods for material property prediction for metallic microstructures while indicating the context and benefit for microstructure-sensitive design. From this, the use of shape moment invariants is offered as solution to quantifying microstructure topology numerically using images. This offers a substantial benefit for computational time since image data is converted to numeric values. The goal of quantifying the image data is to help index grains based on their crystallographic orientation. Additionally, individual grains are isolated in order to investigate the effect of their shapes. After the microstructures are quantified, two methods for identifying the grain boundaries are proposed to make a more comprehensive approach to material property prediction. The grain boundaries as well as the grains of the quantified image are used to train artificial neural networks capable of predicting the material properties of the material. This prediction technique can be used as a tool for a microstructure-sensitive approach to design subtractively manufactured and Laser Engineered Net Shaping (LENS)-produced metallic materials.

# New Computational Methodologies for Microstructure Quantification

Richard K. Catania

(GENERAL AUDIENCE ABSTRACT)

Material properties are dependent on the underlying microstructural features. This work proposes numerical methods to quantify topology and grain boundaries of metallic microstructures by developing physics-based and data-driven techniques for subtractively manufactured and Laser Engineered Net Shaping (LENS)-produced materials.

# Dedication

*This work is dedicated to my wife and parents. Thank you for the unconditional and relentless love and support. This could not have been done without you.*

# Acknowledgments

# Contents

# List of Figures

# List of Abbreviations

$\eta$        Normalized central moment

$\omega$        Dimensionless shape moment invariant

$\phi$        Hu moment

$\theta$        Direction of intensity gradient

$A_g$        Grain area

$A_t$        Total area

G        Magnitude of intensity gradient

ODF        Orientation distribution function

VF        Volume fraction

# Chapter 1

# Introduction and Review of Literature

## 1.1 Material Manufacturing in the Aerospace Sector

Reliable analysis of material manufacturing is critical to pushing the boundary of the state-of-the-art innovations in the aerospace sector. There are a variety of technical and economic considerations when it comes to advancements in manufacturing of aerospace materials, including functional performance, lead time reduction, lightweighting, complexity, cost management, and sustainment [1]. These objectives are not only similar, but they also have interdependent relationships, especially between design and economic goals. Advancements on technical aspects often have a significant impact on the economic aspects. Given the high risk and technical requirements of aerospace applications, the materials used must be complex, reliable, and high performing. The manufacturing of these materials is a high cost process due to the cost of both the materials needed as well as the tools used for manufacturing. Conventional subtractive manufacturing techniques are the standard currently used for most aerospace fabrication. Subtractive manufacturing offers advantages for low complexity and high volume production parts, but as the complexity of manufacturing increases, these techniques become less optimal economically [1]. The repeatability with minimal variation as a result of the manufacturing process is a primary advantage of subtractive manufacturing techniques. The cost of manufacturing can be reduced by increasing the lightweighting of parts, but this leads to an increase in design complexity. When it comes to manufactur-

ing of highly complex materials, additive manufacturing is becoming an increasingly viable option because parts are made layer by layer. The additive manufacturing techniques can also reduce the time needed for production of these more complex components [1]. It offers design teams the ability to optimally distribute the material mass, thus reducing the overall weight of the component. Additionally, additive manufacturing methods reduce the amount of material needed to produce a certain part since it is not subtracted from a larger material. Subtractive manufacturing estimates a ratio of 20:1 for mass of material needed to mass of part produced [2]. This ratio indicates a lack of efficiency for subtractive manufacturing in more complex designs, resulting in an economic disadvantage. For comparison the ratio of material needed for part production using additive manufacturing is between 1:1 and 3:1 [3, 4]. This difference presents a notable economic advantage for additive manufacturing techniques due to the efficient use of materials. Another contributor to the economic advantage of additive manufacturing methods is the reduced need for highly specific tools and fixtures [5]. These tools and fixtures add to the cost of time needed for part production. While additive manufacturing has significant economic and temporal benefit, it has traditionally been used primarily for prototyping rather than production of critical parts [6]. This is likely due to the strict quality standards required for approval in the aerospace sector [7, 8]. additive manufacturing is a relatively new manufacturing process compared to subtractive manufacturing and, as a result, produces a wider range of potential material properties requiring more research to improve reliability and repeatablility of production [9, 10]. To gain a deeper understanding of the effect of processing parameters for additive manufacturing techniques, there exists a need to develop a more reliable way to quantify and interpret experimental material data in order to specify a range of expected material properties and performance. Additively manufactured materials leads to more complex microstructure topologies as a result of the underlying thermo-mechanical processing of the material. To gain a better understanding of the performance of aerospace components fabri-

cated with newer techniques such as additive manufacturing, it is necessary to characterize their microstructural feature such as crystallographic texture and grain topology.

### 1.1.1 Micro-Scale Material Analysis

When investigating the behavior of materials, it is advantageous to analyze its microstructure. Microstructural analysis can shed light on how a material will work on a macro-scale. The design process of aerospace elements can be influenced by understanding the effects of how the materials are formed in the micro-scale. The micro-level design process can be visualized below in Fig. 1.1.
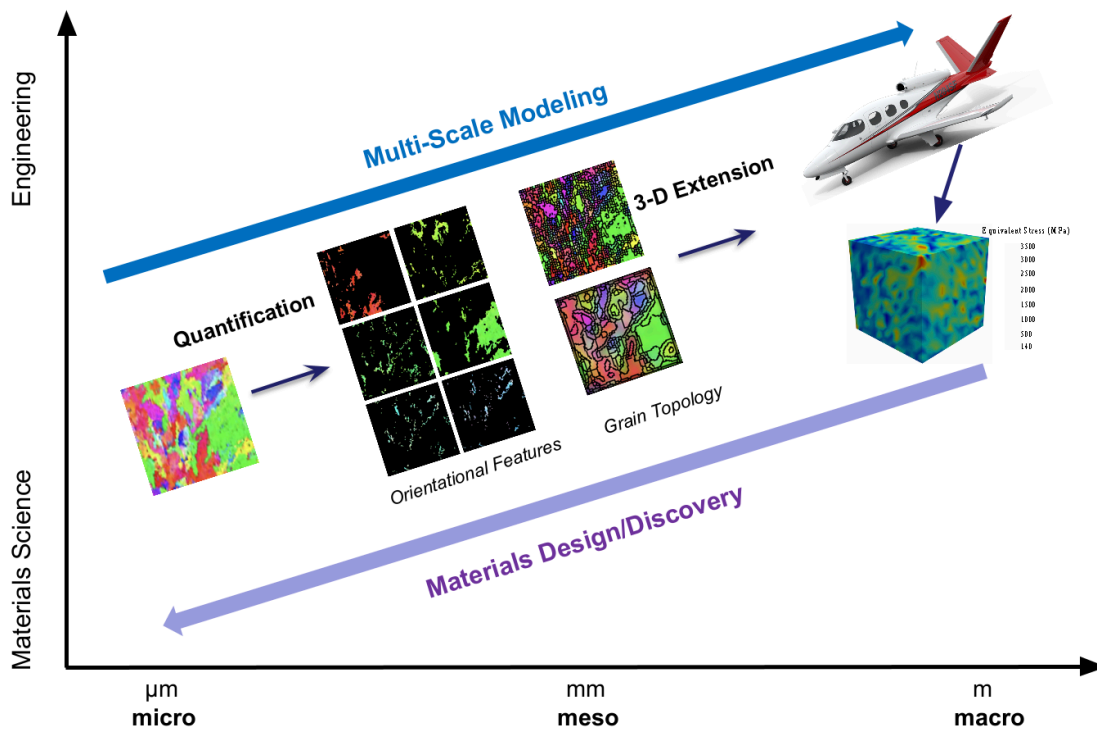


Figure 1.1: Overview of multi-scale modeling and material design processes.

The process of multi-scale modeling involves starting at the smallest scale, for example the micro-scale in the case of this work. During the manufacturing process, newer techniques such as additive manufacturing give the ability to have control over the design of microstructural

features [11, 12, 13, 14, 15]. Having control on the microstructural features of a material would allow greater control over macro-scale properties such as residual stress, porosity, and texture [11, 12, 13, 14, 15]. However, it is necessary to identify and understand the variables related to processing and material composition as well as their relationship to the resulting microstructure [11, 12, 13, 14, 15]. The microstructural features that impact the macro-scale material properties are classified as crystallographic texture and grain topology [16, 17, 18, 19, 20]. Grain topology refers to the size and shape of the grains as well as the boundaries that exist between grains. There have been previous studies that model the crystallographic texture of metals. They aim to capture the percentages of different textures as well as the shapes of different grains in a given microstructure [18, 19, 20, 21]. Although there are numerous publications modeling the crystallographic texture of a microstructure, there are few models that numerically characterize and model grain topology in order to investigate the impact on homogenized material properties in great detail [22, 23, 23, 24, 25, 26]. The effect of how a material is made can be analyzed on the micro-scale and can then be designed to satisfy its performance objectives. As a result, this work aims to develop a physics-based and data-driven framework to explicitly characterize the effects of grain topology on material properties of components, by studying a test-case for an aerospace-grade Titanium-Aluminum alloy.

The experimental method for characterizing materials on the micro-scale comes electron backscatter diffraction (EBSD). EBSD techniques are implemented in conjunction with a scanning electron microscope (SEM), allowing the user to determine and identify the individual grain orientations, local texture, point-to-point orientation correlations, and phase distributions [27]. Gaining insight on these properties can help predict how the material can be used to accomplish a designer's goals. The way in which the grains are shaped and oriented have an effect on the overall properties [28, 29, 30, 31, 32]. The interactions

between different indiviual grains is of interest to material scientists. There have been numerous studies investigating the effect of grain shapes on material properties. Results have shown that properties such as ultimate strength are clearly dependent on the orientation and shape of the grains [34, 35]. Materials have shown to be stronger for both tension and compression along the longest grain axis when compared to the shorter axis [34, 35]. This is an important design consideration especially for additive manufacturing where factors such as build direction and grain directionality can be controlled or at least observed. An area of interest in microstructural analysis is the grain boundary that exists between adjacent grains. It has been shown that the presence of grain boundaries in a material can have a significant impact on the expected properties of structure [36, 37, 38]. Representation of the grain boundary and its inclusion in the prediction of material properties is relatively new, and has mostly been applied to single phase metallic materials [36]. As a result, there needs to be a reliable and efficient way to identify the grain boundaries in a variety of materials, both conventionally forged and additively manufactured, and include the grain boundary in the prediction of material properties.

## 1.2 Objectives of Work and Research Advancements

Based on a review of literature on current microstructural analysis studies, this work will aim to make the following advancements to the field:

- Quantify grain topology of polycrystalline materials

- Computationally characterize and separate crystallographic orientations using k-means clustering.

- Index and isolate singular grains for quantification with Hu moments for both conventionally forged and LENS-produced microstructures.

- Develop two novel methods for identifying the grain boundary of a microstructure

- Prove feasibility of grain boundary identification techniques for both conventionally forged and LENS-produced materials

- Predict properties by developing a data-driven model of microstructure with articifial neural network (ANN)

- Explore the uncertainty associated with ANNs and compare to other, existing methods

- Determine the optimal grain boundary identification technique for those proposed in this work

# Chapter 2

# Quantification of Microstructural Texture and Topology

This chapter will explore the quantification of microstructure images by using a specific type of shape moment invariants called Hu moments for topology and clustering for texture and grain isolation. Some methods and techniques proposed in this chapter have been submitted as a journal article to AIAA Journal: Catania, R., A. Senthilnathan, and P. Acar, "New Methodologies for Grain Boundary Detection in EBSD Data of Microstructures", AIAA Journal, under review.

## 2.1 Capturing Grain Topology in EBSD Images with Hu Moments

Microstructural orientations are typically visualized using EBSD [28, 29, 30, 31, 32]. An example of a typical color EBSD image of a Titanium-Aluminum alloy (Ti-7Al) can be found in Fig. 2.1. The Euler angle used in the EBSD data for this microstructure and all subsequent microstructures is 5 degrees.

(a)                   (b)
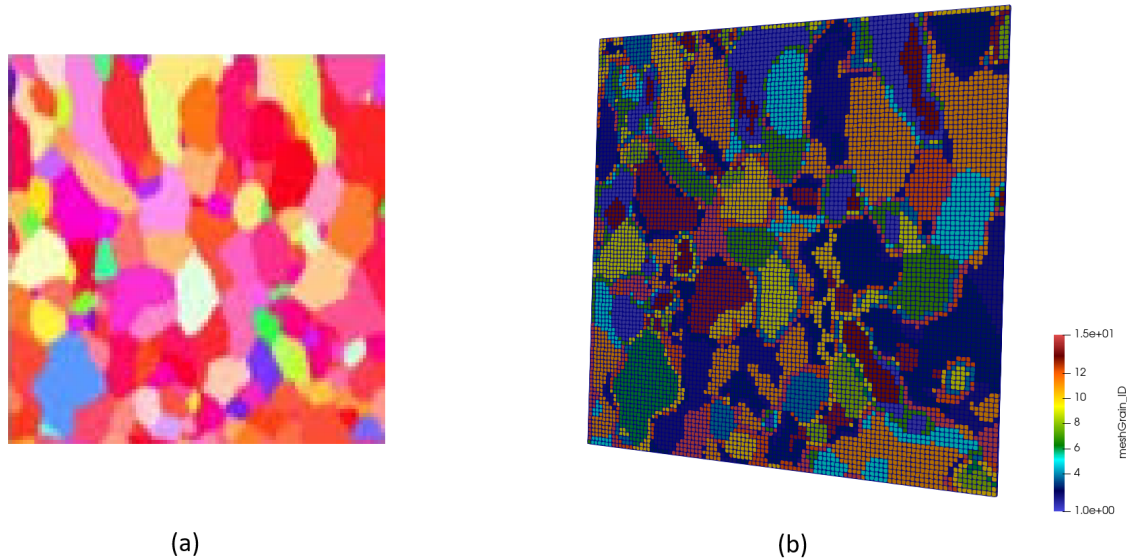
Figure 2.1: (a) EBSD image of a conventionally forged Titanium-Aluminum alloy as is used in this work for quantification. (b) EBSD image that highlights the spectrum of pixel intensity values.

Images can be quantified using image moments, the base of which are raw moments. These moments are calculated using the pixel intensity values in each pixel location. For a grayscale image, there is only one color channel which can have intensity values that range from 0 to 255, where 0 is black and 255 is white. This can be extended to three color channel (RGB) images, where 0 is still black but 255 now refers to the maximum intensity of the specific color in the color channel. When all three color channel values are 255, the pixel is white. The use of raw image moments allow for the calculation of the centroid of the image [39]. For color images, these calculations are done for each color channel separately. From this, it is possible to calculate the central moment for each pixel by comparing it to the centroid obtained from the raw moments. Central moments are beneficial because they are invariant to translation [39]. When the central moments are normalized based on the order of the moment, they become invariant to scale and translation. Ming-Kuei Hu proposed a methodology of combining these normalized central moments to obtain image moments

that are invariant to translation, rotation, and scale [39]. Central moments are second order moment values and represent variance. When normalized, they become third order moment values and represent skewness [39]. The first two Hu moments ($\phi_1$ and $\phi_2$) are derived from the second order normalized central moments ($\eta_{20}$, $\eta_{02}$, and $\eta_{11}$) [39]. The remaining five Hu moments come from different combinations of third order normalized central moments with the exception of $\phi_6$, which includes both second and third order normalized central moments. The mathematical definitions of these seven Hu moments can be visualized below [39]. (2.1)-(2.7):

$$\phi_1 = \eta_{20} + \eta_{02} \tag{2.1}$$

$$\phi_2 = (\eta_{20} - \eta_{02})^2 + 4\eta_{11}^2 \tag{2.2}$$

$$\phi_3 = (\eta_{30} - 3\eta_{12})^2 + (3\eta_{21} - \eta_{03})^2 \tag{2.3}$$

$$\phi_4 = (\eta_{30} + \eta_{12})^2 + (\eta_{21} + \eta_{03})^2 \tag{2.4}$$

$$\phi_5 = (\eta_{30} - 3\eta_{12})(\eta_{30} + \eta_{12})[(\eta_{30} + \eta_{12})^2 - 3(\eta_{21} + \eta_{03})^2]$$
$$+ (3\eta_{21} - \eta_{03})(\eta_{21} + \eta_{03})[3(\eta_{30} + \eta_{12})^2 - (\eta_{21} + \eta_{03})^2] \tag{2.5}$$

$$\phi_6 = (\eta_{20} - \eta_{02})[(\eta_{30} + \eta_{12})^2 - (\eta_{21} + \eta_{03})^2]$$
$$+ 4\eta_{11}[(\eta_{30} + \eta_{12})(\eta_{21} + \eta_{03})] \tag{2.6}$$

$$\phi_7 = (3\eta_{21} - \eta_{03})(\eta_{30} + \eta_{12})[(\eta_{30} + \eta_{12})^2 - 3(\eta_{21}$$
$$+ \eta_{03})^2] - (\eta_{30} - 3\eta_{12})(\eta_{21} + \eta_{03})[3(\eta_{30} + \eta_{12})^2 \tag{2.7}$$
$$- (\eta_{21} + \eta_{03})^2]$$

where $\eta$ refers to the normalized central moments of various orders, denoted by the numeric subscripts [40].

To begin, the entire set of seven Hu moments were used to quantify the texture and grain topology for a given microstructure sample. This work aims to quantify not only the crystallographic texture of the microstructure, but also the texture of the isolated grain boundary network in Titanium-Aluminum alloys, as seen in Fig. 2.2.
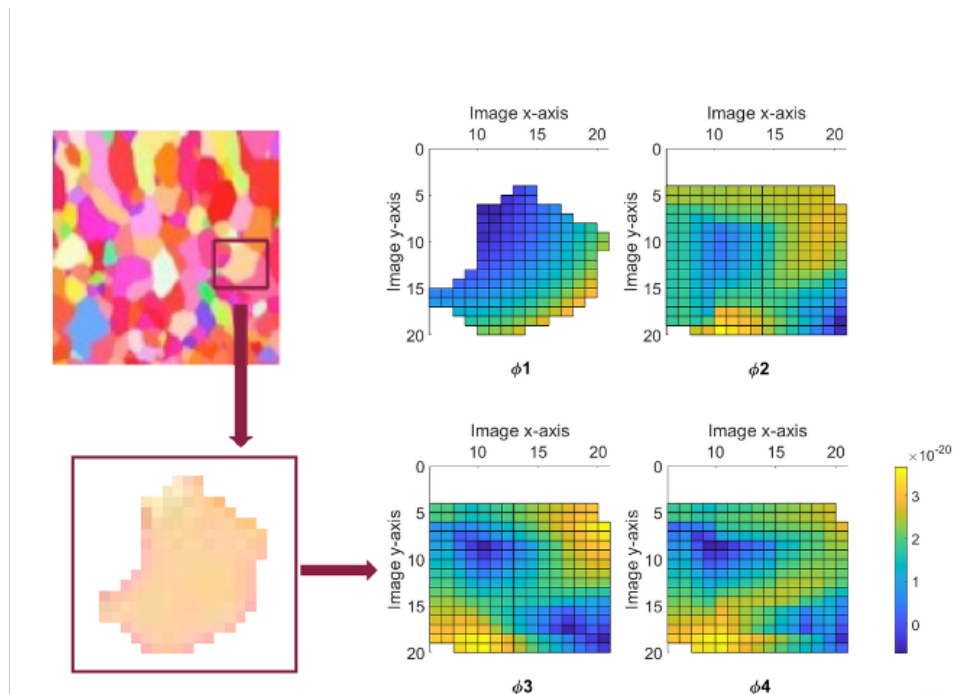


Figure 2.2: Hu Moment calculation for selected grains of a forged Ti-7Al microstructure sample [40].

The seven Hu moment values are determined for each individual pixel of the microstructure, and the first four Hu moment plots can be seen in Fig. 2.2. The final seven moment values of the entire microstructure are determined by the combination of those for each pixel.. The $\phi_1$ plot in Fig. 2.2 shows the shape of the individual grain because Eq. 2.1 does not include a covariance prediction. Additionally, as the Hu moment number increases from one to seven, the magnitude of the calculated value decreases significantly. It is important to determine which Hu moments will drive the material property prediction. This question will be addressed by a sensitivity analysis on each Hu moment as well as uncertainty propagation

in the prediction of material properties. Through Hu moment quantification, it becomes possible to specifically analyze the grain shape of grains with the same texture. Additionally, it will be possible to look at the shape of the grain boundary network. The grain boundary around an individual grain is shown in Fig. 2.2 by the discolored edges around the grain . When quantifying the entire microstructure, it will also be possible to create cumulative network of the grain boundary.

## 2.2 Capturing Crystallographic Texture and Isolating Individual Grains using Clustering

Assume that a single grain image is separated from a randomly oriented microstructure with a pixel area, $A_g$. Traditionally, material properties can be determined based on the orientation distribution function (ODF). The ODF values, which relate to the volume density of each crystallographic orientation in a microstructure sample, can be calculated through the pixels using the following expression:

$$ODF = \frac{VF}{q} \text{ where } VF = \frac{A_g}{A_t} \tag{2.8}$$

$VF$ is the volume fraction comprised of the area of the grain ($A_g$), the total area of the microstructure ($A_t$). The value $q$ refers to the volume normalization vector of the orientation space [40]. For a microstructure, the volume fraction and the ODF values will be the same for all grains. Since pixel intensity values range from 0-255, noise is possible in microstructure image data. Therefore, it is necessary to set a noise threshold for the grains. This threshold is defined as 40 pixels in accordance with a previous iteration of this work. Identified grains with less than 40 total pixels will be treated as noise [40].

For material property prediction of microstructures, the volume fraction of each crystallo-

graphic texture is determined. This work uses a technique called k-means clustering. This method groups pixels into a predetermined number of groups which are centered a mean intensity value. Pixels are divided into these groups based on a user-defined number of mean values, or clusters, within the allowed range of pixel intensity values. To visualize this process, fifteen clusters were defined, and every pixel in the sample image was grouped into the cluster that had its closest mean value, as is seen in Fig. 2.3 [40].
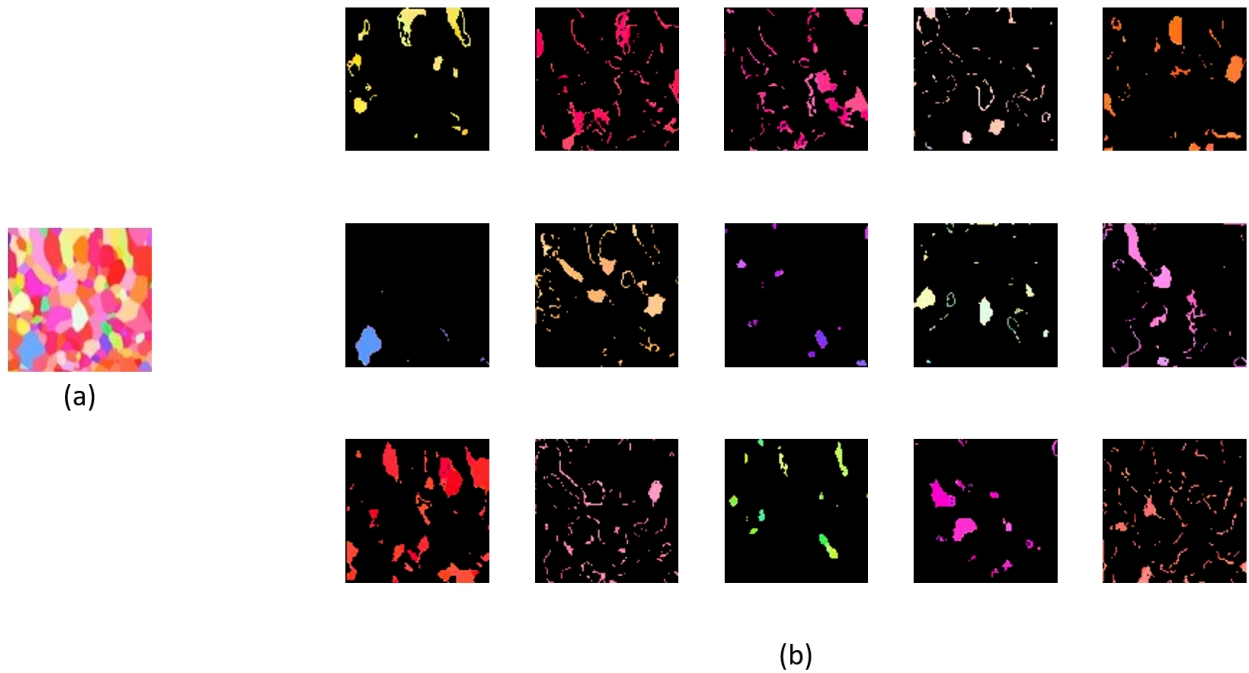


Figure 2.3: (a) Original experimental image of a conventionally forged crystallographic microstructure, (b) Separation of 15 clusters with each cluster indicating a unique microstructural grain orientation [40].

Once the unique grain orientations are partitioned, it is possible to calculate $A_g$ for each cluster in order to find the volume fraction. These values can then be used to predict material properties via the ODF method [40]. However, the hexagonal close-packed crystallographic structure of the Ti-7Al can be modeled in the Rodrigues-Frank orientation space using 50 ODF values [41].

This clustering process can additionally be applied to an LENS-produced polycrystalline sample. The LENS-produced sample also underwent heat treatment after production. Although the conventionally forged grains have more distinct boundaries, the clustering method is still effective in separating the different crystallographic textures for the LENS-produced sample, as can be seen in Fig. 2.4.
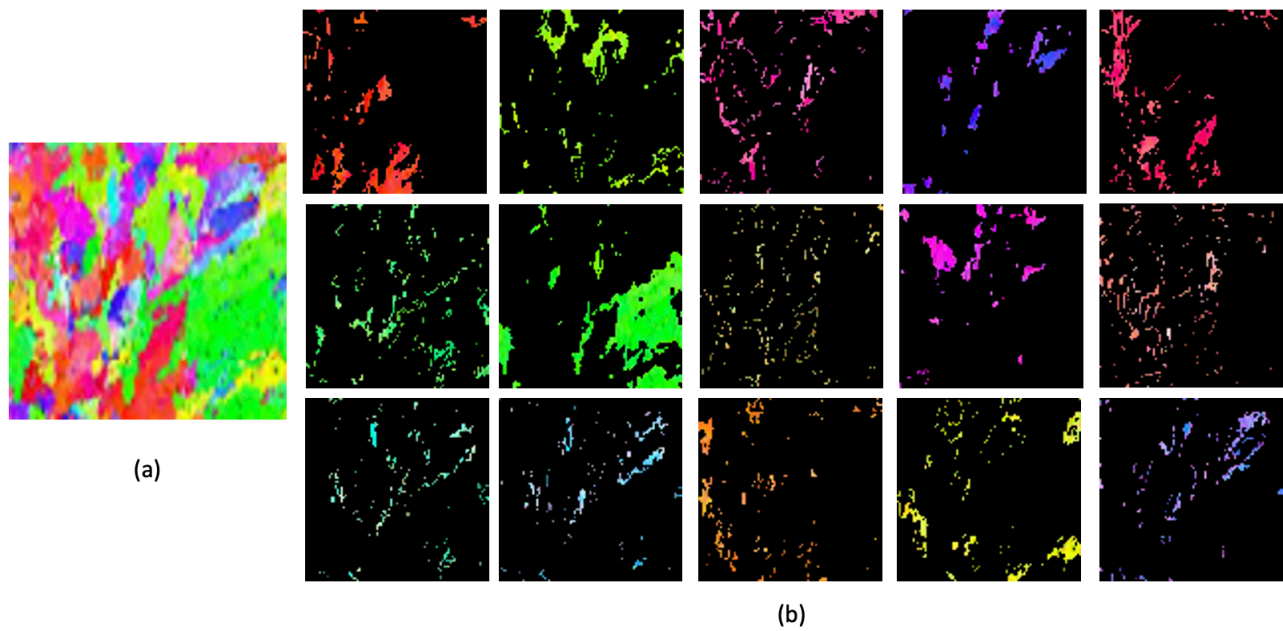


Figure 2.4: (a) Original experimental image of an LENS-produced Ti-7Al alloy, (b) k-means clustering method of separating crystallographic textures where k = 15 [40].

Though this is effective for determining the volume fractions of different crystallographic textures, Hu moments cannot be applied to groupings of grains. Therefore an additional step is required to isolate individual grains. For the purpose of investigating the shape of individual grains, the number of clusters was returned to fifteen because this value produces observably sized grains. The clusters shown in Fig. 2.3 and Fig. 2.4 were indexed based on their respective Red-Green-Blue (RGB) intensity values, then each cluster image was converted to a binary image. The locations where a grain is present is given a value of one, and all other locations are given a value of zero. From this, each individual grain is separated

from others by grouping neighboring pixels with values of one. In order to quantify grains of significant size, a noise threshold of 40 pixels was defined, meaning grains consisting of less than 40 total pixels were neglected. The result of this for both the conventionally forged and LENS-produced samples can be seen in Fig. 2.5 and Fig. 2.6 which uses one of the clusters from Fig. 2.3 and Fig. 2.4 each. For the two selected clusters, the noteworthy grains are isolated.
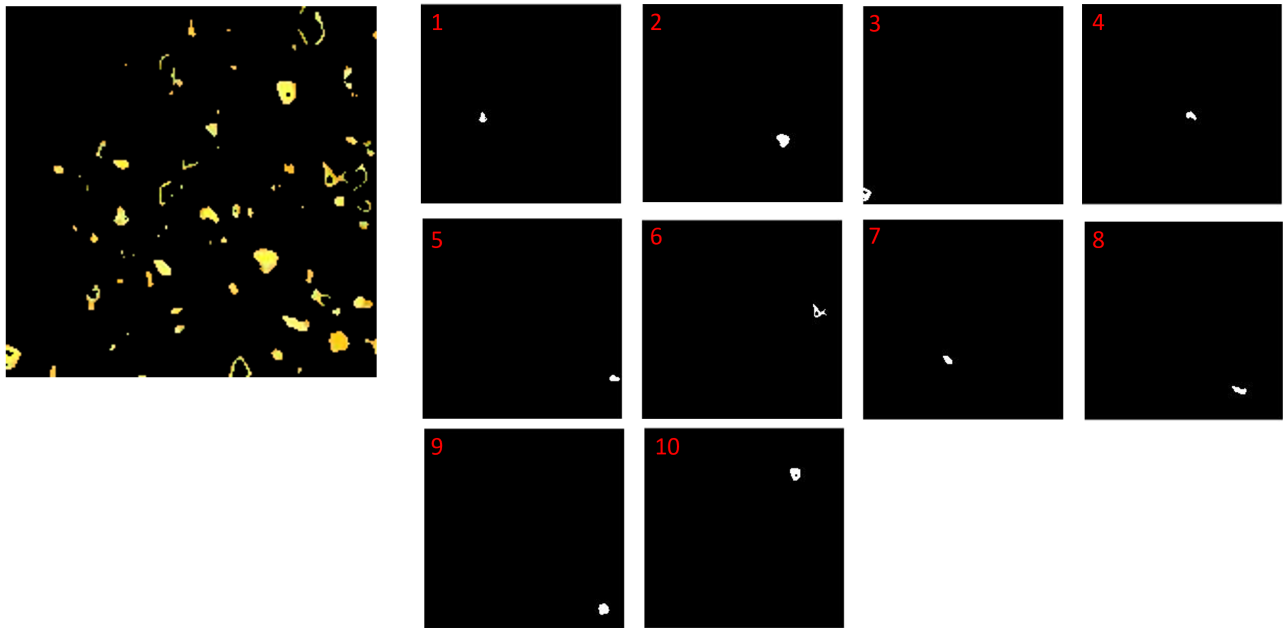


Figure 2.5: Separation of individual grains from a clustered conventionally forged sample based on grain orientation [40].

As can be seen in Fig. 2.5, there are ten large distinct grains that are separated from the clustered image. Similarly, this process is repeated for the LENS-produced sample, as seen in Fig. 2.6. Here, it is possible to see five distinct grains that are isolated from the original clustered image. Each of these grains can then be quantified using Hu moments. Microstructure quantification of both grain shape and crystallographic texture can help when predicting and comparing the properties of the material.
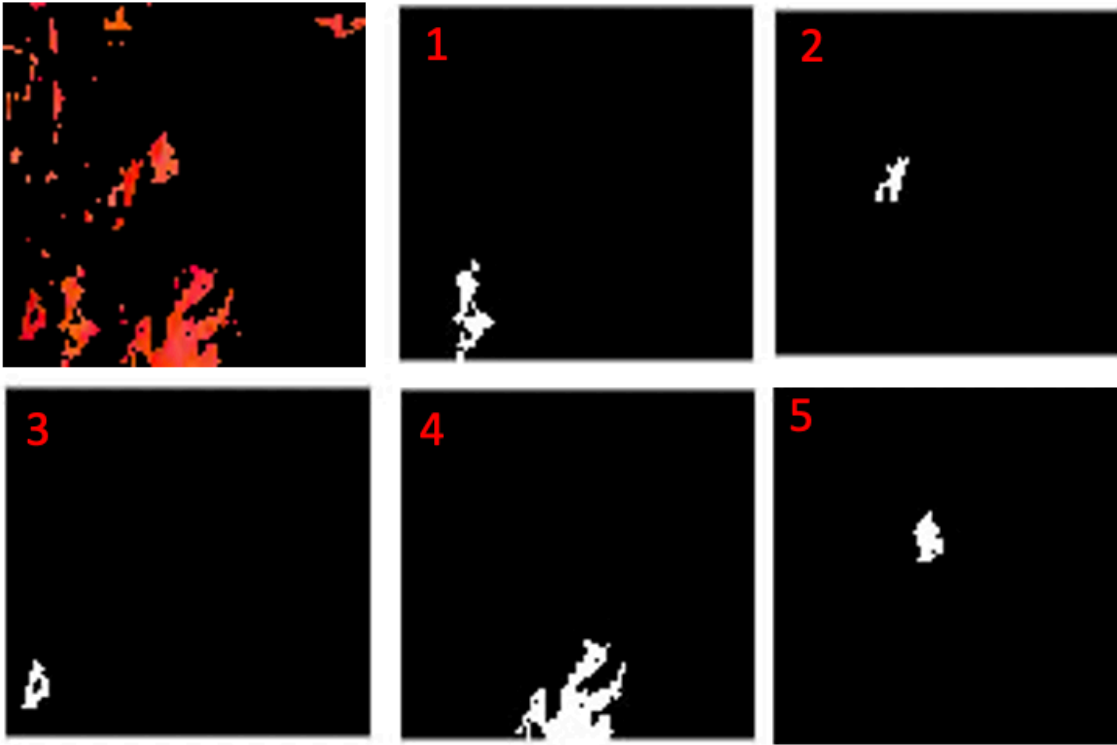
Figure 2.6: Separation of individual grains from a clustered LENS-produced sample based on grain orientation.

The differences of the seven Hu moments for the numbered grains found in Fig. 2.5 can be seen in Fig. 2.7. As can be seen, each individual grain from the conventionally forged sample is quantified differently according to its unique shape. This quantification of individual grains is applied to LENS-produced samples as well, as can be seen in Fig. 2.8. Here, the grain numbers correspond to those shown in Fig. 2.6. Though each of these grains belong to a certain grain orientation, the difference in shape could impact the material properties. For example, equiaxed grains could have different effects on the material properties than columnar grains.
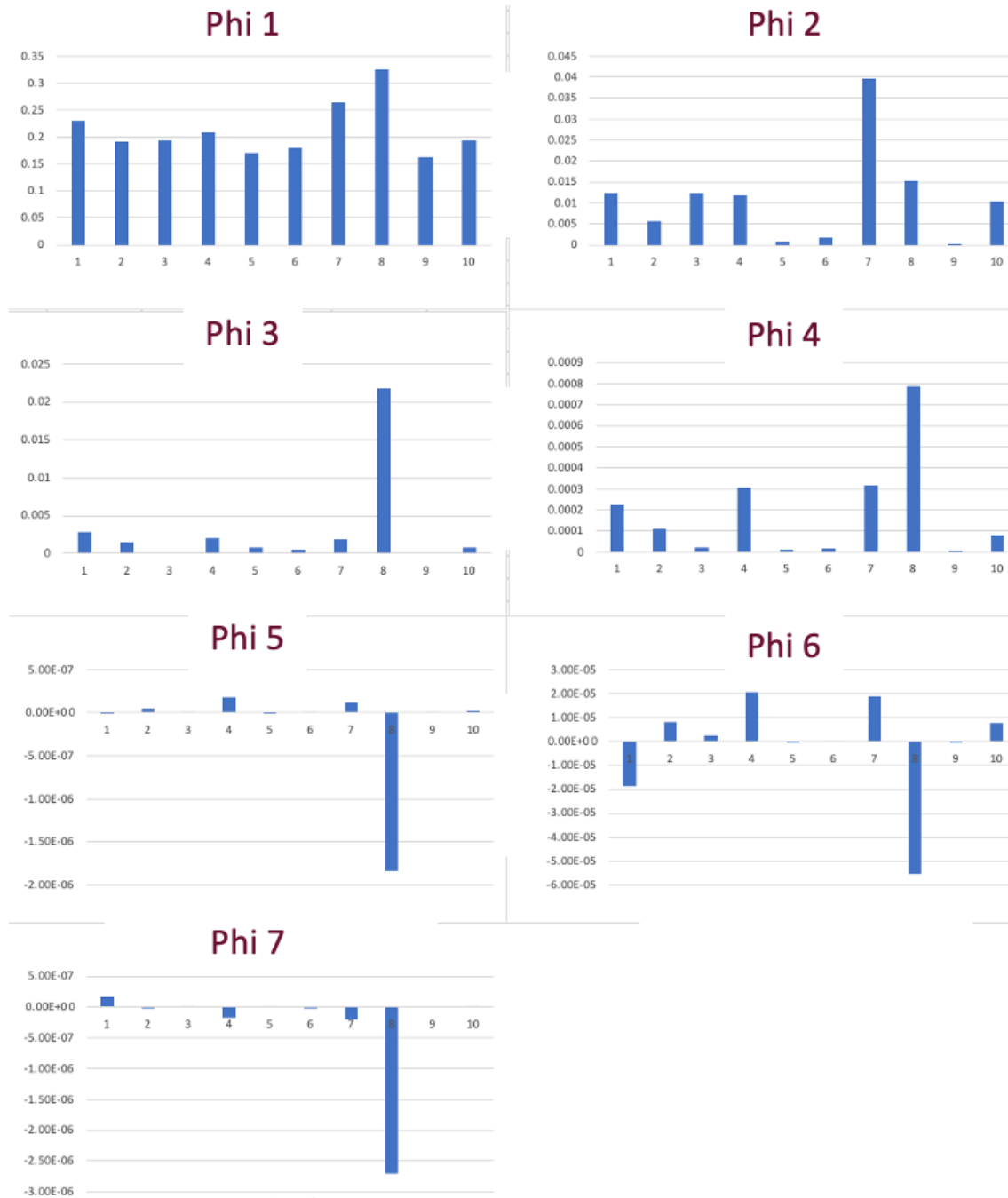
Figure 2.7: Hu moment quantification of ten individual grains from the conventionally forged sample with the same orientation [40].

The recognition of different shapes using Hu moments can also be seen in LENS-produced

grains, as seen in Fig. 2.8.
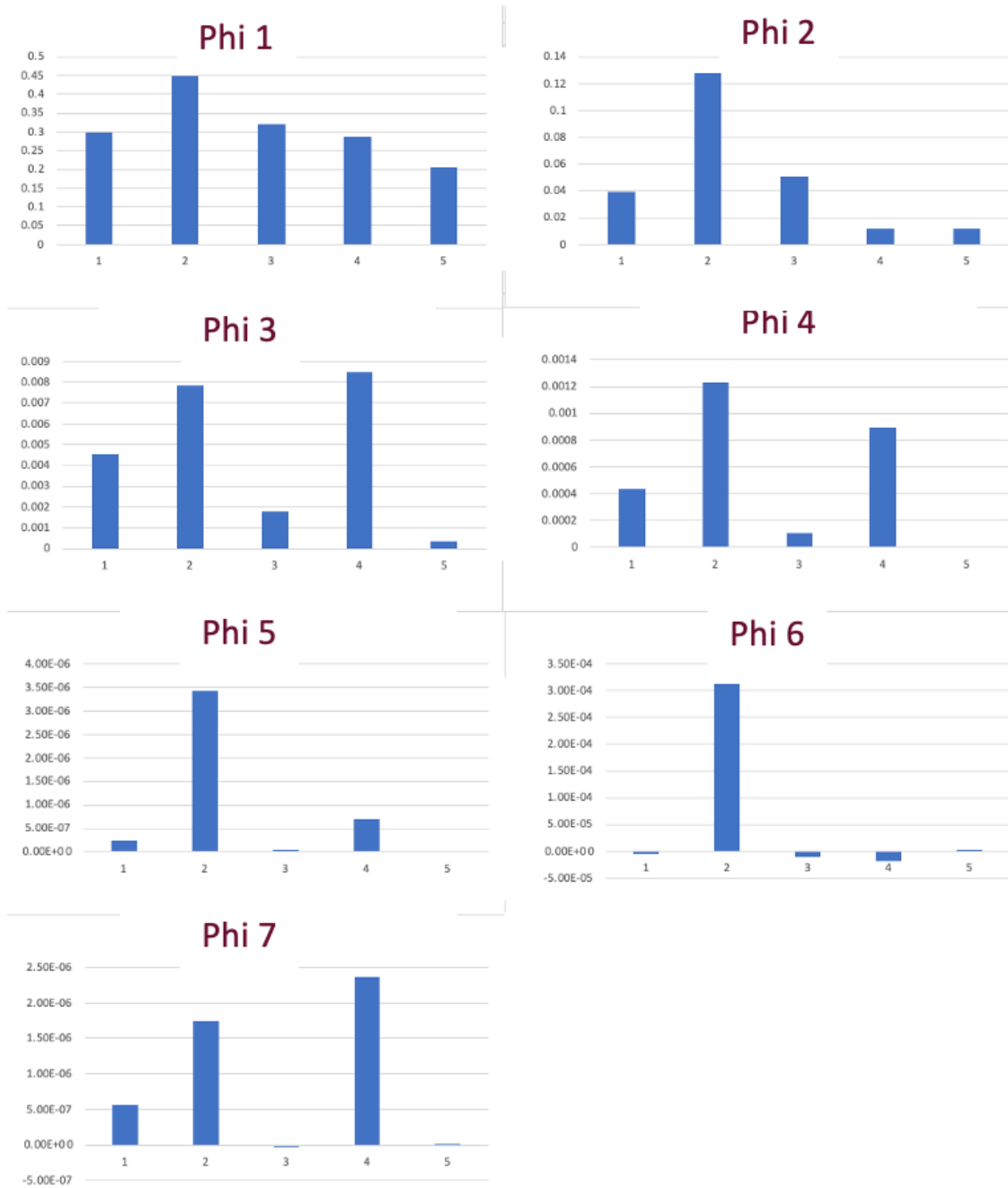


Figure 2.8: Hu moment quantification of five individual grains from the LENS-produced sample with the same orientation.

Applying this method to different manufacturing methods shows the viability of using the

physics-based approach of numerical charaterization and modelling of grain topology.

This can be extended to obtain the material properties of three-dimensionally reconstructed microstructures. For example, Using Markov Random Field (MRF), three dimensional microstructures can be synthesized using cross-sections corresponding to the three axial planes [42]. MRF can help create a volumetric microstructure from two-dimensional input data [40]. To do this, the method used for two-dimensional data discussed above can be applied to data of cross-sections that exist along the three axial directions.
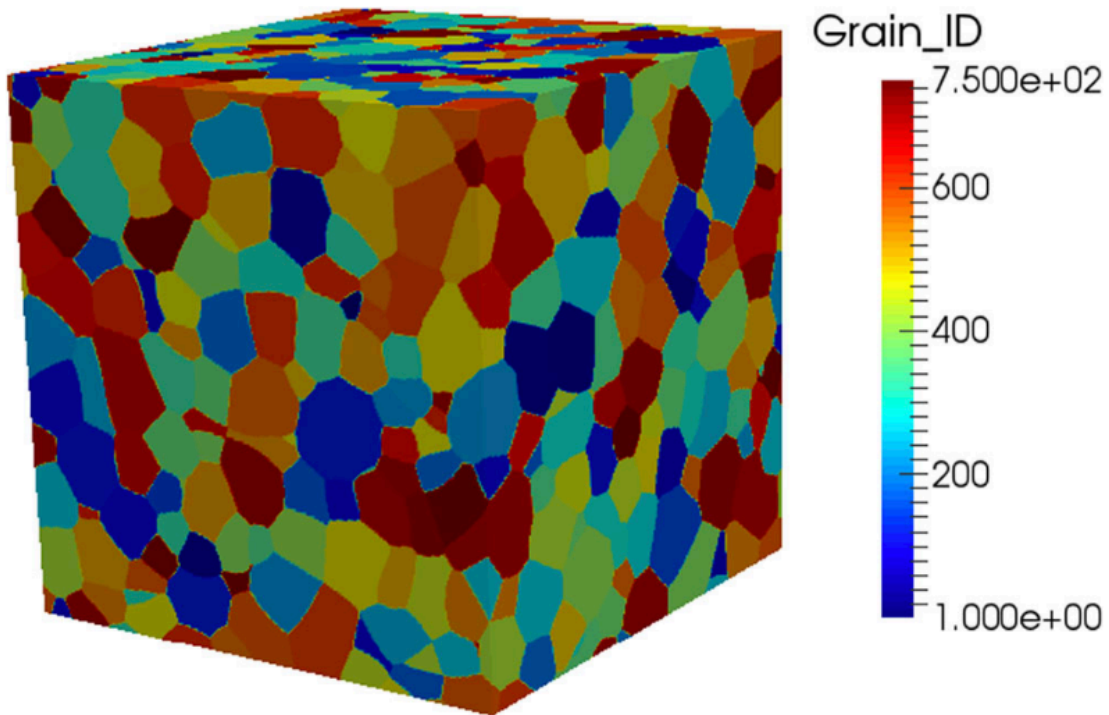


Figure 2.9: Example of three-dimensional microstructure where the cross-sectional approach could be applied [43, 44].

This process can be seen in Fig. 2.9 where the top image shows the three-dimensional image of a polycrystalline microstructure. The process that can be used involves analyzing cross-sections of one pixel depth that lie along the Z-plane. Then, the microstructure data

for the three-dimensional grain topology and crystallographic texture can be constructed by examining the continuity of neighboring two-dimensional microstructure cross-sections. It is important to investigate how the grains change through in three-dimensional space. Quantifying three-dimensional grains can help provide a more complete understanding of how the grain shape and crystallographic texture can affect material properties. Additionally, three-dimensional synthetic microstructure representations (as the example shown in Fig. 2.9) lead to higher fidelity computations of material properties. Therefore, investigating three-dimensional grain topology by extending the proposed methodology is foreseen as a future growth area in computational materials engineering

# Chapter 3

# Detection of Grain Boundaries in Polycrystalline Microstructures

This chapter will discuss the two novel methods devised to identify and quantify the grain boundary in a given microstructure. Some methods and techniques proposed in this chapter have been submitted as a journal article to AIAA Journal: Catania, R., A. Senthilnathan, and P. Acar, "New Methodologies for Grain Boundary Detection in EBSD Data of Microstructures", AIAA Journal, under review.

## 3.1   Exploration of Two Novel Numerical Methods

In order to effectively quantify EBSD data, it is necessary to detect the grain boundaries that separate one grain from their neighboring grains. This work proposes two different methods that offer a comprehensive approach compared to the existing approaches [24, 34, 36**?** ]. These two methods combine the benefits of the different existing grain boundary detection techniques by preserving the crystallographic texture found in the RGB image, indexing individual grains, creating a quantified network of the grain boundary, and isolation of both individual grains and grain boundary.

The first method is called tolerance-based neighbor analysis using the pixel intensity values in each of the RGB color channels [40]. Every pixel in a microstructure image has an intensity value which is calculated by combining the intensity values for each color channel. The pixel

intensity values range from 0 to 255. These values are normalized with respect to 255 and are stored for each pixel location. As a result, each grain intensity is between 0 and 1. The tolerance-based neighbor analysis method compares the color intensity values of a given pixel to each of its local neighbors using a user-defined tolerance value that determines whether the pixel belongs the same grain as its neighbors. The selected tolerance value is a 25 % difference for each color channel. When a pixel has an intensity value that is more than 25 % different than a neighbor in any of the three color channels, it is marked as a grain boundary. With this method, it is possible to detect the clear boundaries between grains in a polycrystalline microstructure as seen in Fig. 3.1.



**(a)**                          **(b)**                          **(c)**
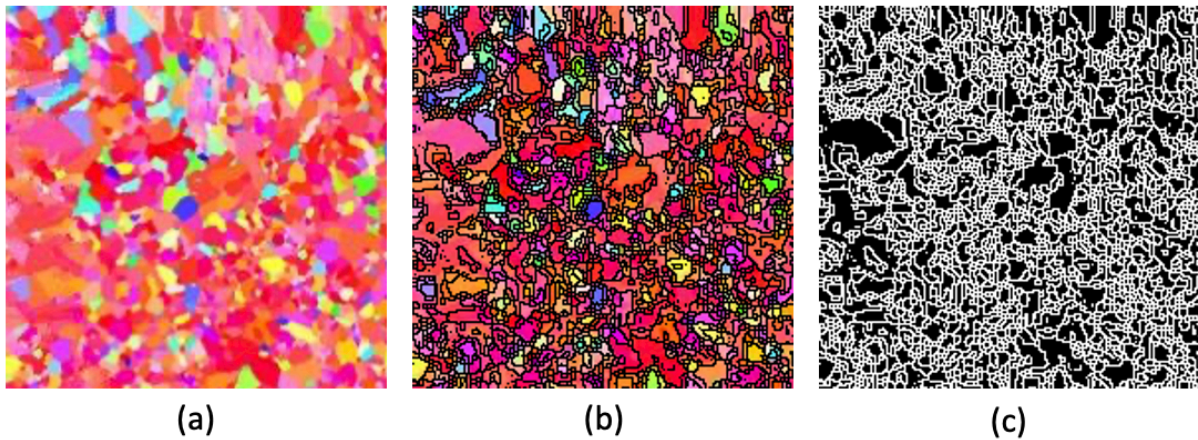
Figure 3.1: Tolerance-based neighbor analysis determination of the grain boundary network of a conventionally forged Ti-7Al sample where (a) is the original microstructure image, (b) is the overlay of the grain boundary on the original image, and (c) is the isolated grain boundary network [40].

To visualize the boundary, the pixels that are considered to be part of the grain boundaries are converted to black. As can be seen in Fig. 3.1, there is a high density of pixels considered to be part of a grain boundary. In order to evaluate the effect of the tolerance threshold, there needs to be some analysis using different tolerance values to optimize the grain boundary detection.

The second method that differs from this tolerance-based technique involves treating each color channel intensity as a coordinate in three-dimensional space [40]. This allows a similarity-based comparison of neighboring pixels. The similarity between neighboring pixels is gauged using Euclidean distance. The result of this method can be seen in Fig. 3.2, using the same sample as seen in Fig. 3.1.
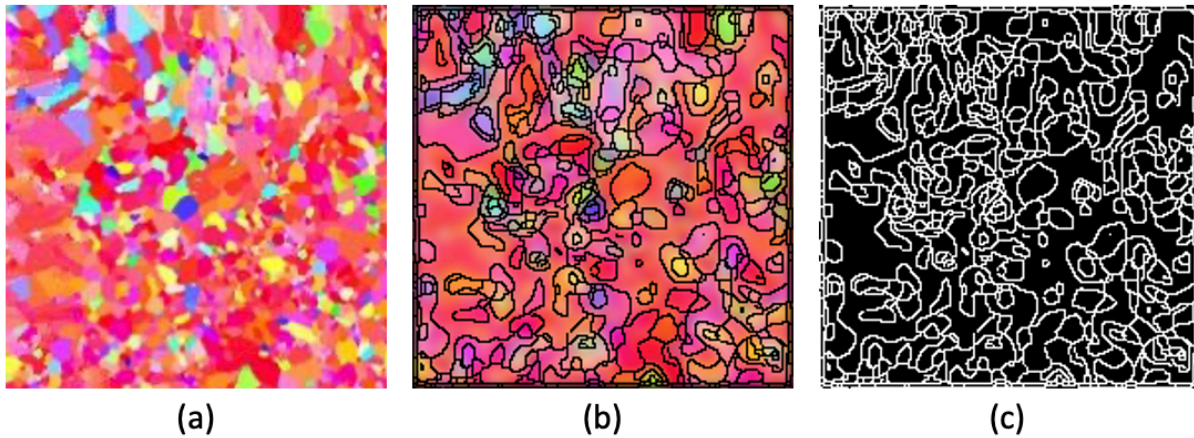


Figure 3.2: Grain boundary identification of a conventionally forged Ti-7Al sample using Euclidean distance similarity where (a) is the original microstructure image, (b) is the overlay of the grain boundary on the original image, and (c) is the isolated grain boundary network [40].

Similarly to the first method, it is necessary to define a maximum acceptable difference between the neighboring pixels. This maximum distance is defined as 1 %. This difference value is substantially smaller than that used in the tolerance-based method because the Euclidean distance values are much closer to each other than the intensity values of the three normalized color channels. Additionally, this small tolerance is also due to the use of a 5x5 Gaussian filter applied before grain detection to smooth the edges between different grains. This is added as an alternative approach to the tolerance-based neighbor analysis method to gauge whether it is advantageous to use a strict identification criteria compared to a criteria aimed to showcase the average orientations of major grains. Although this method presents some difficulty when indexing different grains because of the use of Euclidean distance to

obtain a magnitude across the three color channels, it has the potential to present less noise in each image compared to the tolerance-based method. As can be seen by comparing the grain boundary networks in Fig. 3.1 and Fig. 3.2, the Euclidean distance method contains less grain boundary pixels.

This analysis can also be applied to LENS-produced samples, despite the added complexity. The tolerance-based neighbor-analysis and Euclidean distance methods can be seen in Fig. 3.3.
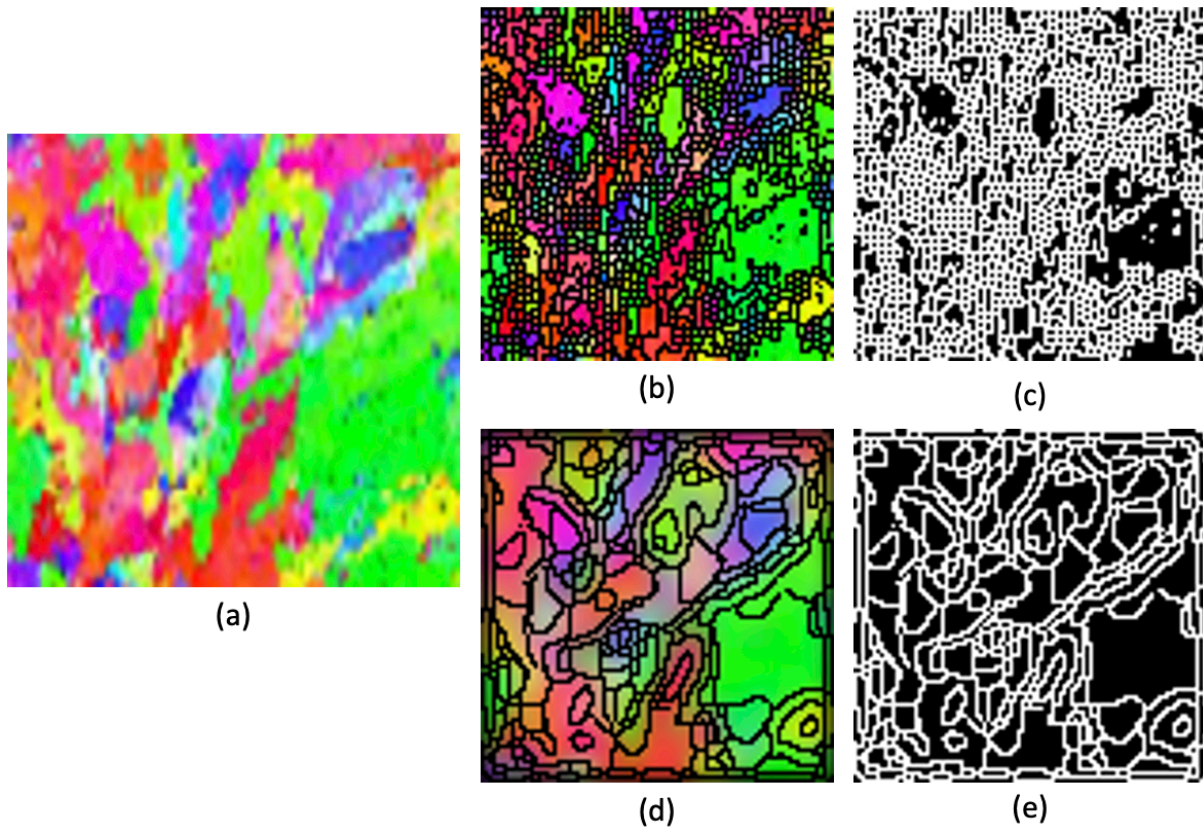


Figure 3.3: Grain boundary identification method comparison of an LENS-produced Ti-7Al sample where (a) is the original sample, (b) is after the tolerance-based neighbor-analysis boundary method is applied, (c) is the network of the grain boundary for tolerance-based neighbor analysis, (d) is after the Euclidean distance boundary method is applied, (e) is the network of the grain boundary for Euclidean distance.

As can be seen, the added complexity of the grains in the LENS-produced sample makes

the tolerance-based neighbor analysis method identify a significant number of pixels as grain boundaries. It is necessary to evaluate whether this is advantageous when predicting material properties.

The advantage of detecting and marking the grain boundary is that it can then be treated as its own orientation, allowing for its inclusion in the calculation of the volume fractions. With the grain boundaries having their own volume fraction, it is possible to include them in the use of ODF, as shown in Eq. 2.8. The volume fraction of the grain boundaries can be included in the overall calculation by using Figs. 3.1(b)-Fig.3.3(b).

In Figs. 3.1-3, it is found that the grain boundaries make up at a minimum 12 % of the total area, depending on the sample and method [40]. This is a significant percentage for each of the microstructure samples. For comparison, a single grain orientation only accounts for a maximum of roughly 11 % of the total sample [40]. The significant presence of the grain boundaries could suggest that it is important to consider when predicting the material properties of the sample.

## 3.2 Comparison of Tolerance-based Neighbor Analysis and Euclidean distance Grain Boundary Detection Techniques to the Canny Edge Detection Method

A common technique used for shape separation in images to which these methods can be compared is the Canny Edge Detector, a tool in Python used for image processing. This tool involves multiple steps beginning with a Gaussian blur to reduce noise in the image [45]. This blur consists of a 5x5 Gaussian filter. Then, the continuity of pixel intensity is gauged by measuring the intensity gradients both vertically and horizontally. Eq. 3.1 shows how the intensity gradients are measured using magnitude (G) and the direction ($\theta$) [45].

$$G = \sqrt{G_x^2 + G_y^2}; \ \ \theta = \arctan{(\frac{G_y}{G_x})} \tag{3.1}$$

where G corresponds to the magnitude of the intensity gradient with $G_x$ and $G_y$ being
the horizontal and vertical components of the intensity gradients, respectively. The term $\theta$
measures the direction of the intensity gradient [46]. The edges are then identified but the
thickness is not consistent. To obtain more consistent edge thicknesses, the Canny Edge
Detector uses non-maximum suppression. First, the local maximum gradient values are
identified. The local maxima of the intensity gradients indicate that they are edges. Any
detected edge pixels that are not local maxima in their respective intensity gradients are
suppressed, thus reducing the thickness of the detected edges [46]. The last step of the
process involves using hysteresis thresholding to preserve the continuity of the edge lines.
This process is done by defining a minimum and maximum threshold. The maximum value
is defined so that any pixel above this threshold is considered a certain edge. The minimum
value is defined so that any pixel that is below this threshold is certainly not an edge. The
maximum threshold value was chosen as the intensity value of 125 out of 255. Whereas,
the minimum threshold value was chosen as the intensity value 50 out of 255. These two
values were defined because they proved to best detect the grain boundaries visually. The
result of applying the Canny Edge Detector was aimed to be similar to that of the Euclidean
distance technique, meaning it was desired to have a less strict detection of the grains that
the tolerance-base method. These threshold values prevent the presence of non-continuous
edges [? ]. The result of applying Canny Edge Detection method on a conventionally forged
polycrystalline microstructure is shown in Fig. 3.4 below.
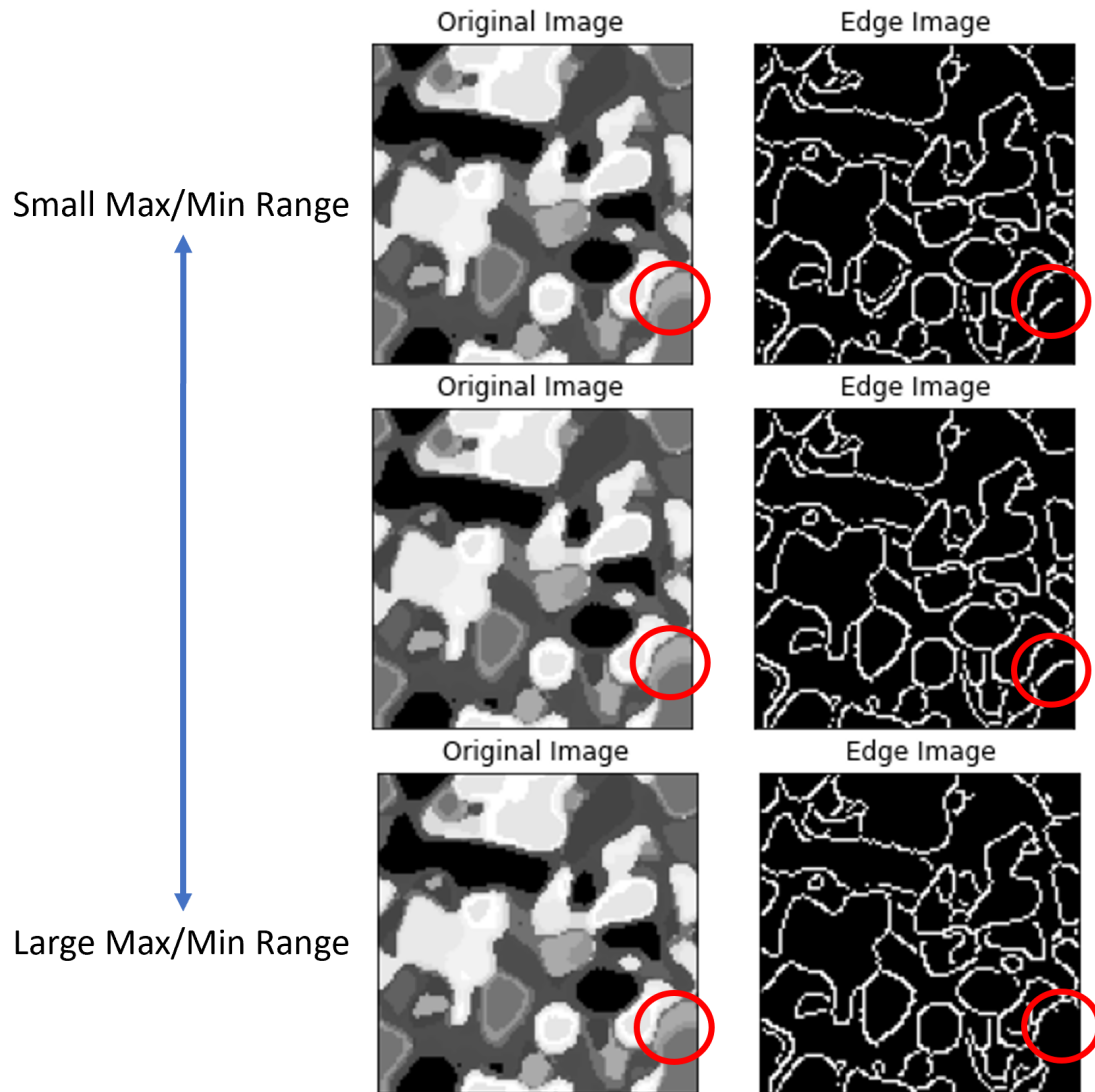
Figure 3.4: Application of Canny Edge Detector on Ti-7Al sample with the Original (grayscale) and the Edge images [40].

As can be seen in Fig. 3.4, the variation in the maximum and minimum threshold values affects the edges identified in this method. An example of these differences can be seen in the area circled in red for each circle. A small range between the two thresholds does not identify the edge in its entirety, whereas a large range does not identify the edge at all. The chosen values 125 and 50 for the respective maximum and minimum values best identified

the grain boundary for the sample microstructure, as seen in the middle image of Fig. 3.4.

It is necessary to note that this method removes the color information because it can only work on a grayscale image. Therefore, it is difficult to preserve orientation information and index different grains according to their texture. Moreover, the Canny Edge Detector needs some trial and error when determining the hysterisis threshold values, making it difficult to get favorable and consistent results for larger data sets. If the thresholds are not well defined, the edges will either not be identified or be grouped inaccurately [46]. The two proposed methods offer benefits over this existing method because they do not have the same disadvantages in terms of consistency, color preservation, and grain indexing. The proposed methods would therefore be better at separating grains to then apply shape moment invariants to obtain shape information of the grains.

The effect of including the grain boundaries when predicting material properties using the proposed two methods will be explored by using them as additional input in a neural network. The tolerance-based neighbor analysis and Euclidean distance similarity methods differ in the strictness by which grain boundaries are identified. To explore the difference between these methods, a binary grain boundary network will be used in conjunction with the original microstructure image. The binary grain boundary networks are shown below in Fig. 3.5, where (a) is a conventionally forged polycrystalline microstructure, (b) and (c) are the binary grain boundary networks obtained using tolerance-based neighbor analysis and Euclidean distance similarity, respectively, (d) is an LENS-produced polycrystalline microstructure, (e) and (f) are the isolated grain boundary networks obtained using the same methodology as (b) and (c), respectively. The actual grains are represented as black pixels, whereas the grain boundaries are shown as white pixels. The grain boundaries are shown in white in order to be the primary focus of the shape moment invariants because they only consider nonzero intensity values.
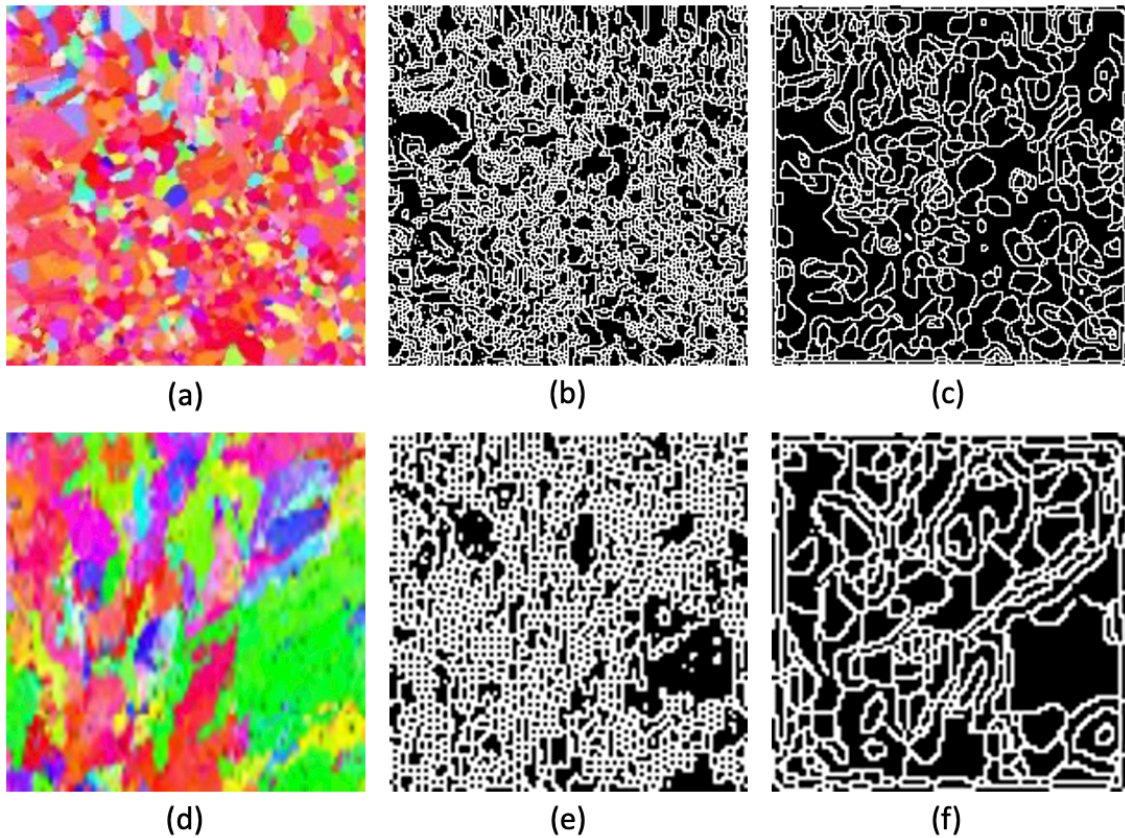
Figure 3.5: Grain boundary network comparison where (a) is the original conventionally forged Ti-7Al sample, (b) is neighbor analysis grain boundary of (a), (c) is the Euclidean distance grain boundary of (a), (d) the original LENS-produced Ti-7Al sample, (e) is the neighbor analysis grain boundary network of (d), (f) it the Euclidean distance grain boundary network of (d).

The grain boundary networks in Fig. 3.5 demonstrate that neighbor analysis method is more strict when differentiating different grains. This is most likely because it directly compares each of the corresponding RGB color channels when separating grains [40]. Meanwhile, the Euclidean distance combines the RGB color channels before conducting comparison, creating an intensity magnitude value instead. Since the pixel intensity values range from 0 to 1, the needed tolerance for Euclidean distance is comparatively small compared to the neighbor analysis method when differentiating grains.

# Chapter 4

# Results and Discussion

This chapter will cover the training of artificial neural networks based on shape moment invariants. Uncertainty analysis is additionally conducted to determine an expected range to which material properties vary. Some methods and techniques proposed in this chapter have been submitted as a journal article to AIAA Journal: Catania, R., A. Senthilnathan, and P. Acar, "New Methodologies for Grain Boundary Detection in EBSD Data of Microstructures", AIAA Journal, under review.

## 4.1 Application of Shape Moment Invariants to Predict Material Properties of conventionally forged Microstructures using Artifical Neural Networks

Two different grain boundary identification techniques were developed to investigate the effect of including grain boundary consideration for predicting the material properties of a microstructure. The methods differ in the strictness to which they define grain boundaries. Both methods create a binary image of the grain boundary network. These grain boundary networks can be seen in Fig. 4.1, where (a) is the original microstructure, (b) and (c) are the networks identified using neighbor analysis and Euclidean distance, respectively [40]. All pixels that are not part of the grain boundary are converted to black pixels to emphasize the location of the grain boundary themselves, shown by white pixels. By showing the network

29

in white, the grain boundary is given a nonzero pixel intensity value so that the Hu moments are calculated according to the grain boundaries themselves.



<div align="center">(a)            (b)            (c)</div>
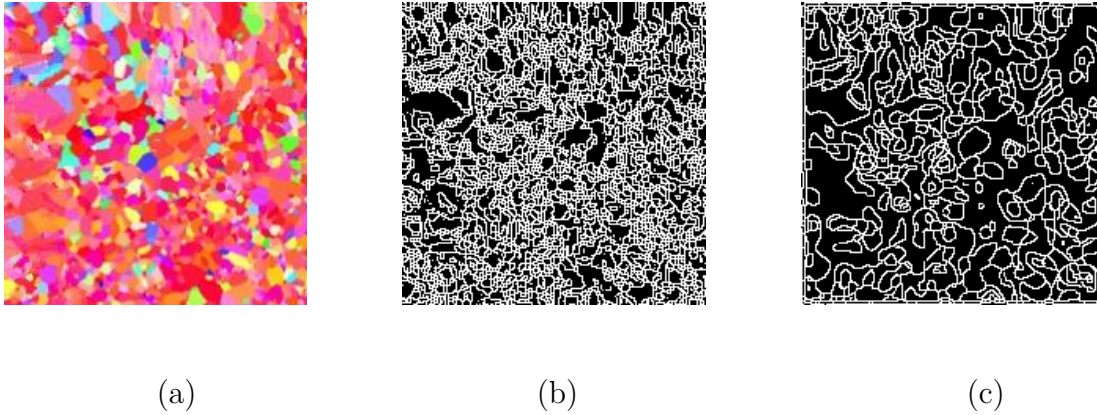
Figure 4.1: Grain boundary filtration where (a) is the original conventionally forged microstructure, (b) is the neighbor analysis grain boundary network (c) is the Euclidean distance grain boundary network [40].

As can be seen from the two networks, the neighbor analysis method considers a significant amount of pixels to be part of the grain boundary, showing it is a strict grain differentiation method. This is because this method compares adjacent grains in each color channel separately. Alternatively, the Euclidean distance method calculates an intensity magnitude using a combination of the three color channels. Since the pixel intensity values range from 0 to 1, the Euclidean distance threshold requires a significantly smaller value to distinguish to which grain it belongs.

After creating the two grain boundary networks, a data-driven model was developed by training neural networks with sample microstructure data to evaluate the effect of the grain boundary identification methods on the prediction of homogenized material properties of the microstructure. A set of 100 conventionally forged Ti-7Al EBSD images was used due to the computational expense of generating additional images synthetically [40]. Due to the limited sample size, the neural network was trained using Bayesian Regularization because it can

generalize well with smaller data sets [47, 48]. Instead of using the sample image as input for the neural networks, the Hu moments of the overall image were used.The definition of neural networks in terms of Hu moments leads to a parametric data-driven model, which is expected to require significant smaller amount of data compared to image-based models. As previously mentioned, the seven Hu moments use the three color channel pixel intensity values to quantify the crystallographic texture of the microstructure. For three color channels, the Hu moments are obtained by averaging the values from each channel. For the binary grain boundary networks, the Hu moments are calculated in only one channel to avoid redundancy. These sets of Hu moments were included as input to give the material properties as output, specifically the Young's modulus values for the x-direction and y-direction as well as yield strength, represented as $E_{11}$, $E_{22}$, and $\sigma_y$, respectively.

In order to assess the predictive quality of using neural networks with the inclusion of the grain boundary network, an initial artificial neural network was trained with Bayesian Regularization, using the Hu moments of the microstructure images in the three color channels [40]. Once this original artificial neural network was trained, two additional artificial neural networks were trained with the inclusion of the two grain boundary networks obtained from the tolerance-based neighbor analysis and Euclidean distance methods, respectively. The artificial neural networks were trained with a set of Hu moments as input as well as corresponding experimental material properties as output. The data set of 100 experimental images was divided into a training set, a validation set, and a test set, respectively accounting for 70 %, 15%, and 15% of the total [40]. The number of hidden layers used for the artificial neural network was chosen to be 8 after testing various hidden layer options. It was found that using less than 8 hidden layers under-fit the data, yielding inaccurate results. Moreover, using more than 8 hidden layers appear to over-fit the data because the artificial neural network did not perform well on the test set.

After obtaining favorable results with the three artificial neural networks, a sensitivity analysis was performed to gauge which Hu moments drove the material property prediction. A 5% change was applied to each of the 7 Hu moments individually to see which ones affected $E_{11}$, $E_{22}$, and $\sigma_y$ the most [40]. As can be seen in Fig. 4.2, the impact of $\phi_1$ was substantially more notable than the other Hu moments when predicting the material properties. A previous study had similar findings relating to the significance of $\phi_1$ due to its much higher magnitude than other Hu moments [49].



<div align="center">

(a)                                        (b)                                        (c)

</div>
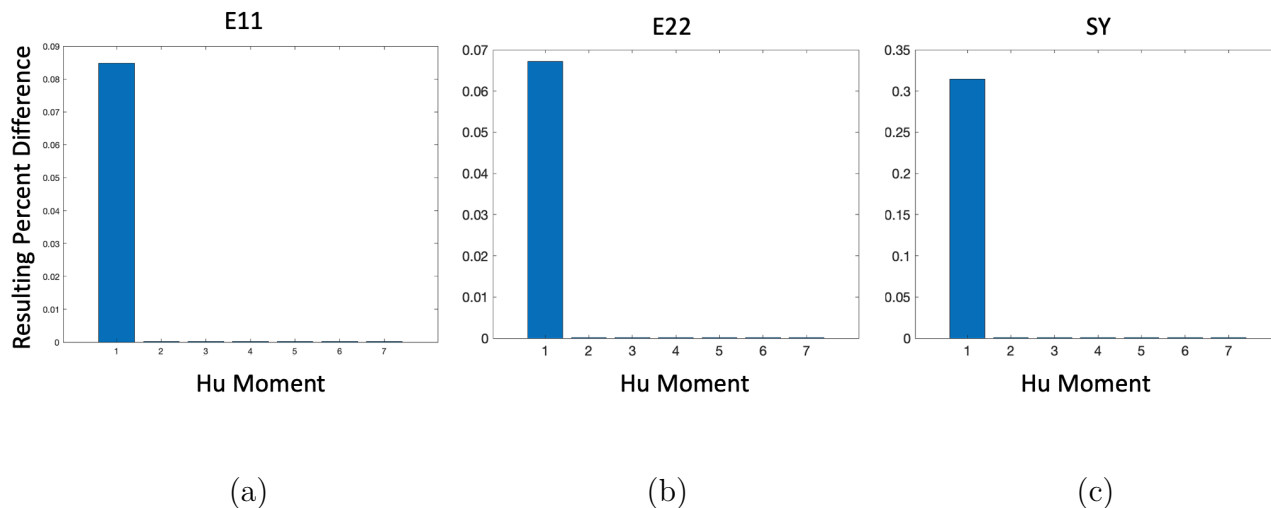
Figure 4.2: Sensitivity analysis showing the percent changes in (a) $E_{11}$, (b) $E_{22}$ , (c)$\sigma_y$ as a result of 5 % changes in individual Hu moments[40].

For $E_{11}$, increasing $\phi_1$ by 5% increased the predicted value by nearly 0.1%. Additionally, a 5% increase in $\phi_1$ showed approximately a 0.1% and 0.3% increase in $E_{22}$ and $\sigma_y$, respectively. While these output increases are smaller than the increase applied to Hu moments, the effect of $\phi_1$ is much more significant than the other Hu moments. $\phi_1$ has a comparatively higher magnitude than the other 6 Hu moments. This can be visualised in Fig. 2.2, where the $\phi_1$ most effectively captures the shape of the grain. Additionally, it is worth noting that yield stress has a larger increase than Young's modulus. This is possibly because the Young's modulus is determined in linear elastic region, while the yield strength is determined in the

elasto-plastic region [40]. This shows that elasto-plastic properties are likely more sensitive to grain topology and grain boundary input.

After the sensitivity analysis, the artificial neural networks were trained again using only $\phi_1$ to focus on the most decisive input variables [40]. The three artificial neural networks were trained using the same parameters as above but only including the first Hu moment of the original image and of the corresponding grain boundary networks as inputs. The regression plots of the three artificial neural networks can be seen in Fig. 4.3.
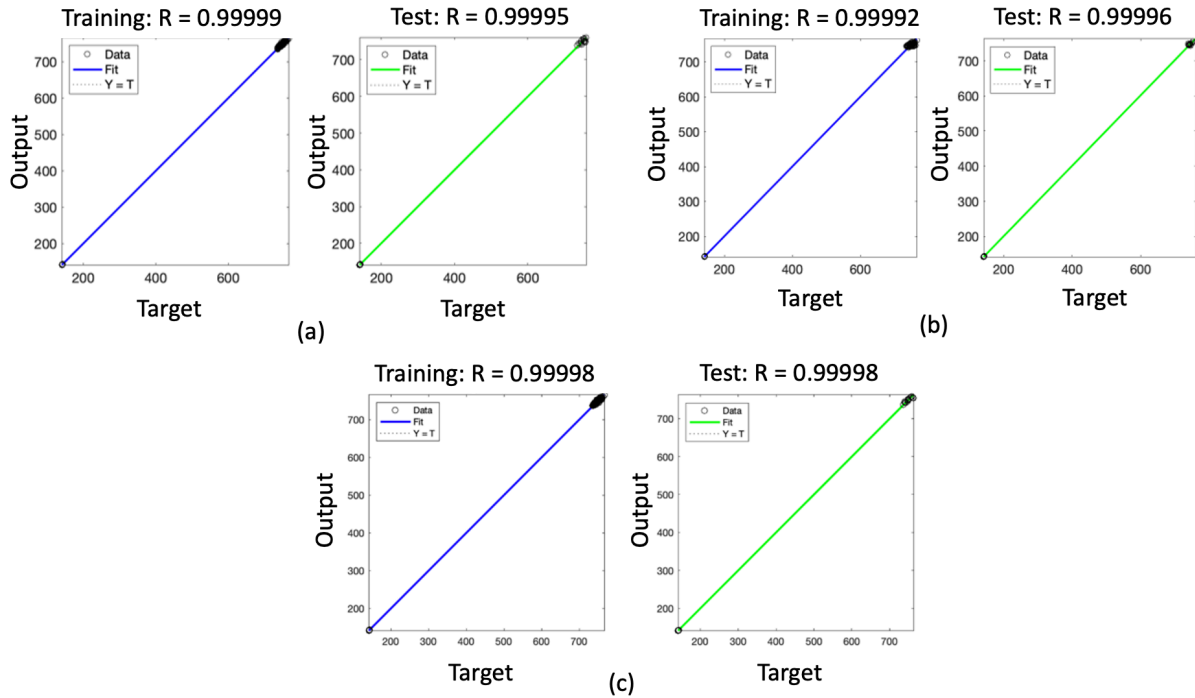


Figure 4.3: Regression results of the aritifical neural networks trained with (a) no grain boundary, (b) neighbor analysis grain boundary, and (c) Euclidean distance grain boundary [40].

As seen in Fig. 4.3, there is good fitting performance for each of the three neural networks for both the training and test sets. From the regression plots, the two grain boundary inclusive methods have a slightly better fit than that of the method that does not include grain boundary consideration. Despite the good fit of the artificial neural networks, it is important

to evaluate the similarity of the material property predictions of the neural networks to the experimentally-obtained properties. From this, it is possible to determine the performance of each artificial neural network. Fig. 4.4 shows the percent difference between the material property prediction of each neural network compared to the experimental properties.
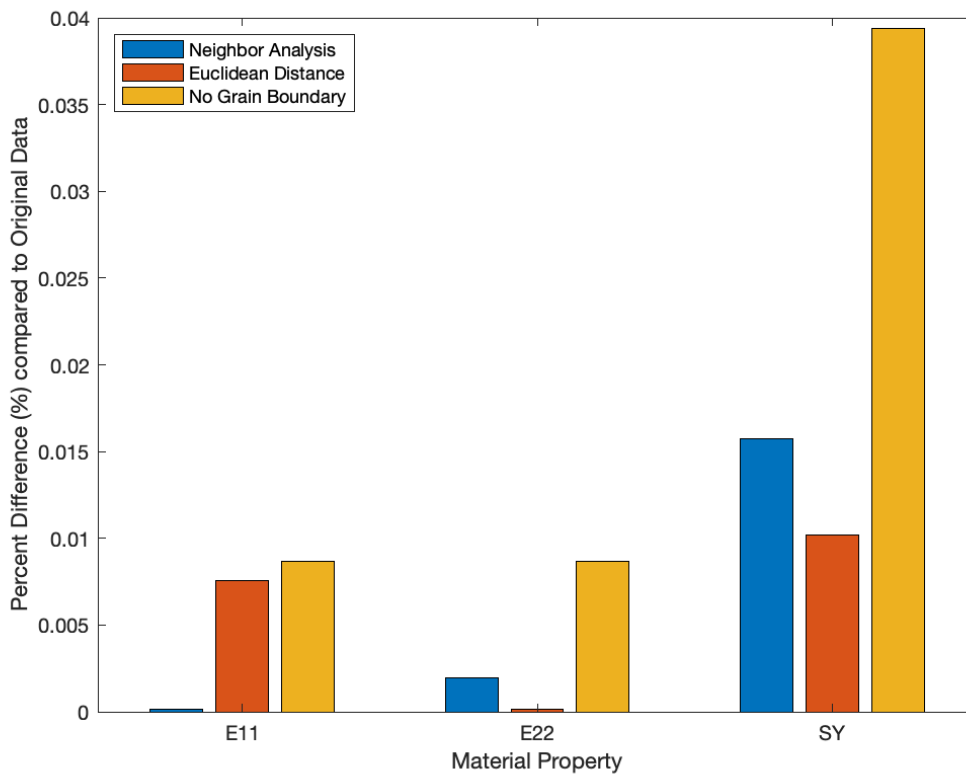


Figure 4.4: Material property predictions compared to experimental data for the two grain boundary inclusive methods as well as the grain boundary exclusive method [40].

The material property outputs of the artificial neural network function that does not consider the grain boundary have a higher percent difference than the grain boundary inclusive networks for all three material properties. Although the no grain boundary method was outperformed, all three neural networks gave favorable Young's modulus predictions less than 0.01 % different than the experimental results [40]. The largest difference between the no

grain boundary method and the grain boundary inclusive methods appeared for the yield stress. The $\sigma_y$ predictions showed the grain boundary inclusive methods outperformed the no grain boundary by a magnitude of roughly 2 and 3 for neighbor analysis and Euclidean distance, respectively. From the conventionally forged samples, it is unclear whether the tolerance-based neighbor analysis method or the Euclidean distance method provides the best results for the prediction of all three material properties because neighbor analysis gave a better prediction for $E_{11}$ while Euclidean distance gave better predictions for $E_{22}$ and $\sigma_y$. It is important to note that the maximum percentage difference for any material property prediction using the artificial neural networks was less than 0.04 %. A previous study that used crystal plasticity simulations yielded a percentage difference of roughly 5 % for the same material properties [50]. This disparity between the artificial neural network predictions and the crystal plasticity predictions is likely due to the model uncertainty of crystal plasticity simulations. For the conventionally forged microstructures, it is possible to see that including the grain boundary network as input leads to an artificial neural network that outperforms one that does not consider the grain boundary network [40]. As previously stated, it is still unclear whether the artificial neural network trained with the tolerance based neighbor analysis or Euclidean distance is the optimal choice for material property prediction. In order to further evaluate the two methods, it will be necessary to investigate the performance of the grain boundary inclusive artificial neural networks on LENS-produced samples.

## 4.2   Uncertainty Quantification of conventionally forged Microstructures using Artificial Neural Networks

When manufacturing materials, processing may lead to inherent material uncertainty that can be quantified using experimental microstructure data samples. In order to simulate this uncertainty with the microstructure samples, a data set was generated from the av-

erage Hu moments of the microstructures. This set consisted of 1000 samples that were normally distributed with a maximum difference of ±5 %. This assumption on the level of microstructure uncertainty is consistent with the preliminary work that investigated the microstructural texture uncertainty for the same data set [51]. The first data set was composed of the Hu moments of the microstructure samples, representing the crystallographic texture. The following two data sets corresponded to the Hu moments of grain boundary networks for the tolerance-based neighbor analysis and Euclidean distance methods, respectively. Fig. 4.5 shows the histograms of these three sets of data. It is important to note that the Hu moments from the RGB microstructure have a non-zero intensity value for nearly every pixel, whereas the grain boundary networks have a significant number of zero-value pixels.



(a)                                   (b)                                   (c)
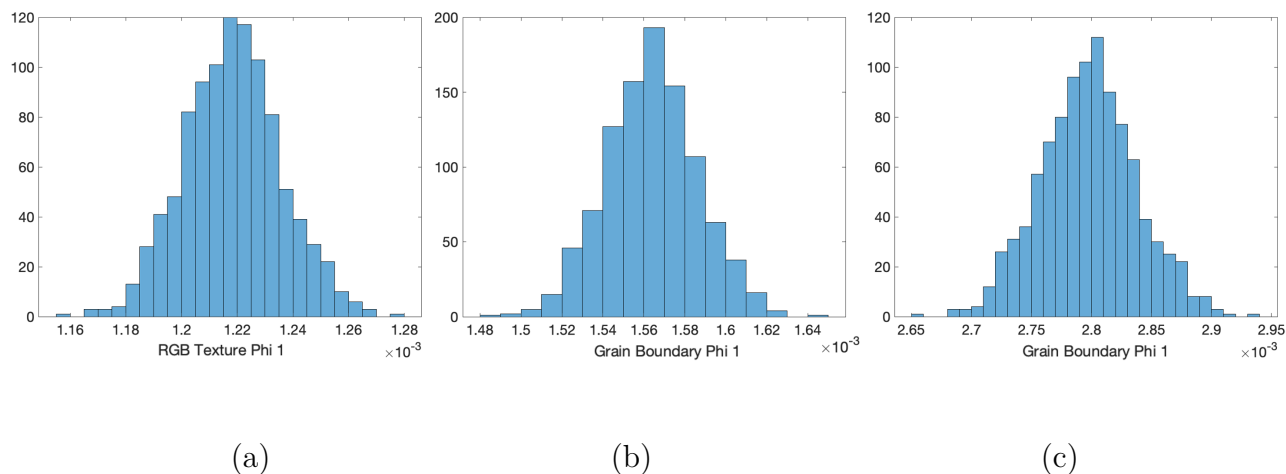
Figure 4.5: Distribution of Hu moments used as ANN input where (a) is $\phi_1$ of the overall RGB image, (b) shows $\phi_1$ of the neighbor analysis grain boundary grid, and (c) shows $\phi_1$ for that of the Euclidean distance method [40].

After generating the normally distributed set of Hu moments, they were used to perform Monte Carlo Simulation (MCS) with the three artificial neural network functions. The predictions of each artificial neural network function for $E_{11}$ can be seen in Fig. 4.6.

|     |     |     |
| --- | --- | --- |
| (a) | (b) | (c) |

Figure 4.6: Distribution of ANN ouput, $E_{11}$, based on normally distributed $\phi_1$ sample inputs obtained using (a) no grain boundary, (b) the neighbor analysis, and (c) Euclidean distance methods [40].

The motivation of this uncertainty analysis is to represent the uncertainty from sample to sample as a result of the manufacturing process. It is important to determine a reasonable range in which the possible material properties can reside. The range of $E_{11}$ outputs are 0.7 GPa, 1.0 GPa, and 0.8 GPa for the no grain boundary method, the neighbor analysis method, and the Euclidean distance method, respectively [40]. The results of $E_{22}$ are consistent with those of $E_{11}$, as can be seen in Fig. 4.7. The distributions for the Young's modulus values are similarly distributed with those of the Hu moments, showing that there is a quasi-linear relationship between the Hu moments and Young's modulus output for each artificial neural network.
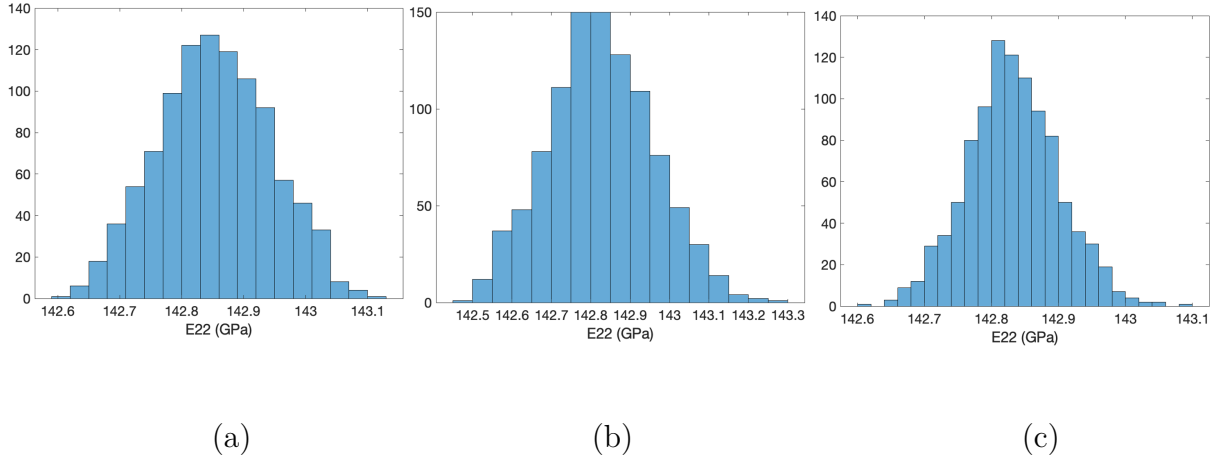
Figure 4.7: Distribution of ANN ouput, $E_{22}$, based on normally distributed $\phi_1$ sample inputs obtained using (a) no grain boundary, (b) the neighbor analysis, and (c) Euclidean distance methods [40].

When considering the distribution of $\sigma_y$, the results of the artificial neural networks are skewed to the left, as can be seen in Fig. 4.8. Additionally the ranges of the $\sigma_y$ predictions are significantly larger than for the Young's modulus. The $\sigma_y$ ranges are 9 MPa for the no grain boundary ANN, 16 MPa for the neighbor analysis ANN, and 8 MPa for the Euclidean distance ANN. Since the $\sigma_y$ predictions are skewed, it suggests that the relationship between the Hu moments and yield stress is more complicated than that for the Young's modulus [40].

(a)                                    (b)                                    (c)
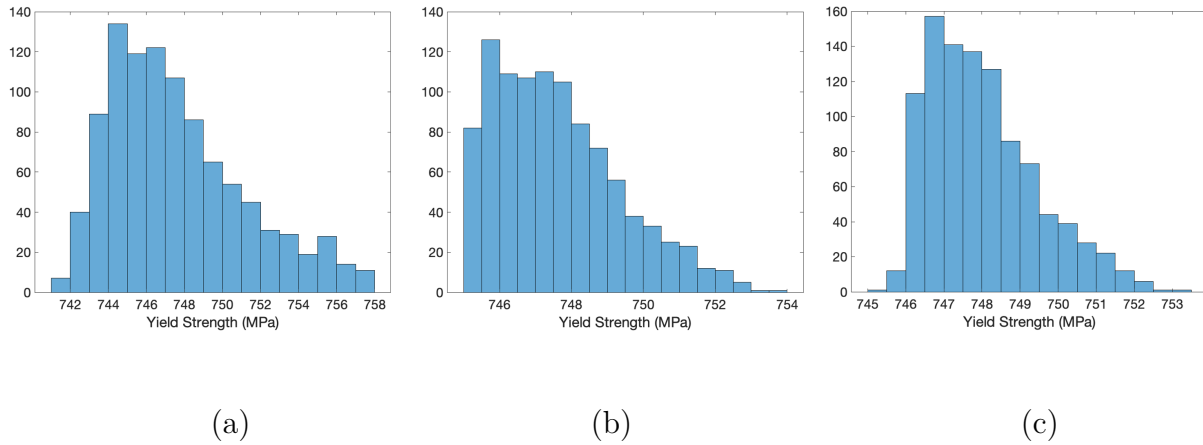
Figure 4.8: Distribution of ANN ouput, $\sigma_y$, based on normally distributed $\phi_1$ sample inputs
obtained using (a) no grain boundary, (b) the neighbor analysis, and (c) Euclidean distance
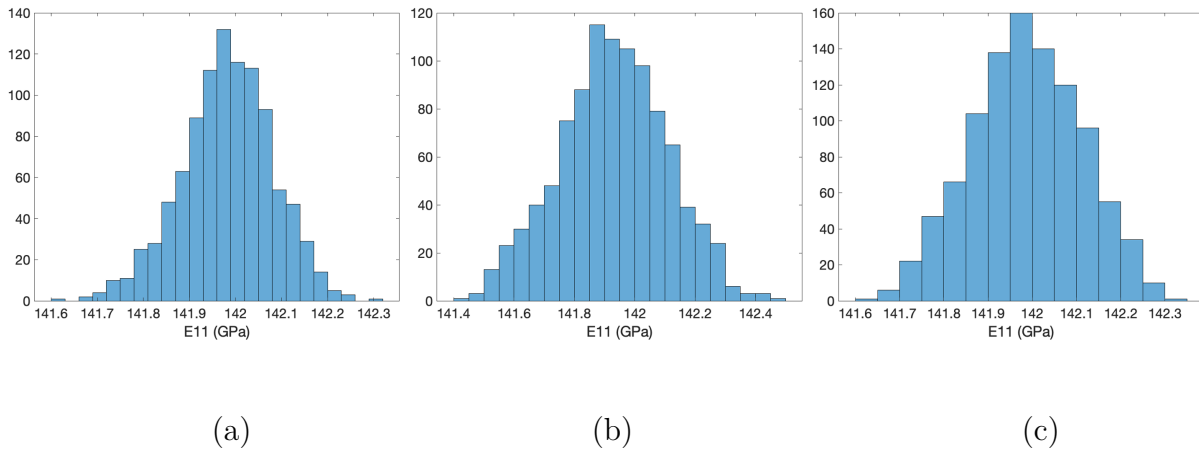methods [40].

This method of predicting material properties of microstructures by quantifying the image us-
ing Hu moments in two-dimensions could be expanded to three-dimensional microstructures
by using the cross-sectional images in different planar directions. The three-dimensional
grain boundary network could also be determined in the same way. However, it would
be necessary to consider the continuity of the grains and grain boundaries by examining
the progression of the cross sections in all three axial directions. Once the continuity of
the three-dimensional microstructure is resolved, it would be possible to use these artificial
neural networks to predict the material properties of a three-dimensional microstructure.

## 4.3 Material Property Prediction of LENS-produced Microstructures using Artificial Neural Networks

After training artificial neural networks for the conventionally forged microstructures above,
it was important to investigate the predictive performance these networks had on LENS-
produced samples. Since there was a lack of experimentally-determined material property
data for LENS-produced samples, the grain boundary inclusive artificial neural networks
trained from the conventionally forged microstructures were used to gauge their effectiveness

for LENS-produced samples. In doing so, it would also be possible to potentially determine which of the two grain boundary inclusive methods had better performance for a wider range of microstructure data. The data set used to evaluate the artificial neural networks consisted of 1000 synthesized LENS-produced Ti-7Al microstructures. The known material properties of this data set was the Young's Modulus and yield stress, obtained using PRISMS Plasticity [52]. For an explanation of PRISMS, see Appendix A.

Similarly to the methodology discussed above for the conventionally forged samples, $\phi_1$ was obtained for each of the overall microstructures as well as $\phi_1$ of each of the tolerance-based neighbor analysis and Euclidean distance grain boundary networks, respectively. Fig. 4.9 shows a sample microstructure as well as the corresponding grain boundary networks.



(a)      (b)      (c)
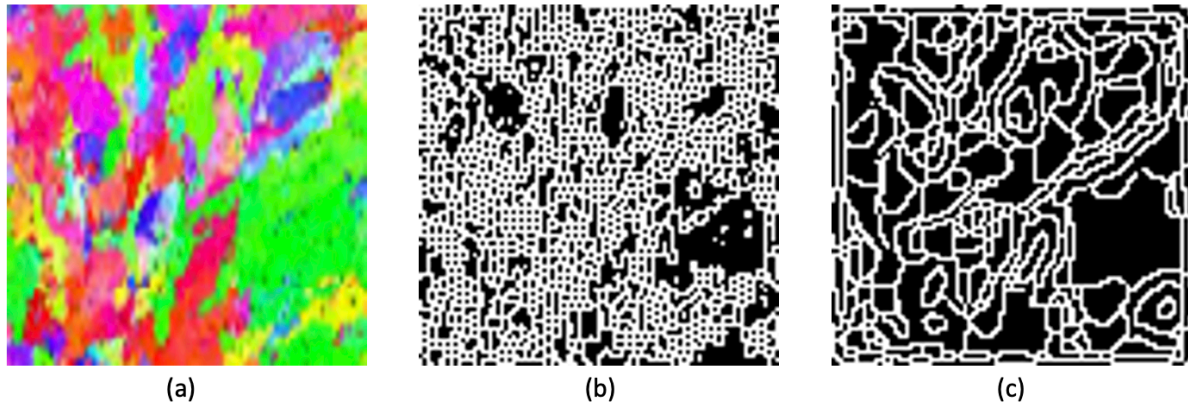
Figure 4.9: Example of LENS-produced image data used to obtain Hu moments for input into the grain boundary inclusive artificial neural networks where (a) is the original microstructure, (b) is the neighbor analysis grain boundary network (c) is the Euclidean distance grain boundary network.

The Hu moments obtained from the microstructure data in Fig. 4.9 were then used as input into the grain boundary inclusive artificial neural networks to evaluate the material property predictions. While there were no experimental Young's modulus values for comparison, the predicted values of approximately 142.6 GPa and 143.4 GPa for $E_{11}$ and $E_{22}$ appear to be similar to those of the conventionally forged samples above. Given that both are Ti-7Al, the

predictions for the LENS-produced samples are reasonable.
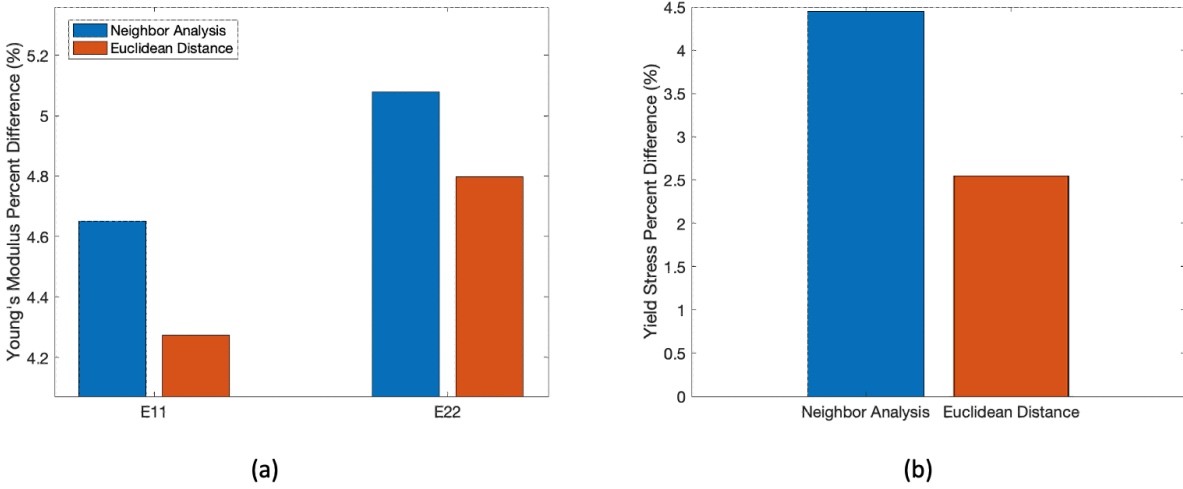


Figure 4.10: LENS-produced material property outputs from the grain boundary inclusive artificial neural networks where (a) is the percent difference of Young's modulus and (b) is the percent difference of $\sigma_y$ compared to crystal plasticity simulations.

As can be seen from Fig. 4.10, the artificial neural networks were able to predict the $E_{11}$, $E_{22}$, and $\sigma_y$ values of the LENS-produced microstructure with less than a 5 % difference to the value obtained from the crystal plasticity simulation. It can be seen that the Euclidean distance grain boundary network gives a value of $\sigma_y$ that has an approximately 2.5 % different value to that of the crystal plasticity simulation. In this comparison of material property prediction, it is found that the Euclidean distance method outperforms the tolerance-based neighbor analysis method, similarly to the case of the conventionally forged microstructure. It is necessary to note that the percent differences of both grain boundary inclusive methods are higher than those of the conventionally forged samples. Since the prediction for all material properties are within 5 %, the higher percent difference of the LENS-produced microstructure could possibly be attributed to the model uncertainty arising from crystal plasticity simulations [50]. The difference between comparison metrics for the conventionally forged and LENS-produced samples are that the material properties of the former were

obtained experimentally, and those of the latter were obtained through crystal plasticity simulations. Despite the higher percent difference seen in the material property predictions for the LENS-produced samples, the results appear to be within expected ranges due to the uncertainty of the crystal plasticity simulations. Additionally, the better performance of the Euclidean distance method is consistent with the conventionally forged case.

## 4.4 Uncertainty Quantification of LENS-produced Microstructures using Artificial Neural Networks

As with the conventionally forged case, there is uncertainty from sample to sample arising from the manufacturing process of LENS-produced samples. To investigate the effect of this uncertainty, MCS was applied to the LENS-produced case. First the average first Hu moments were calculated for the microstructure and both grain boundary networks. From this, 1000 normally distributed samples were created with a maximum perturbation of 5 %.
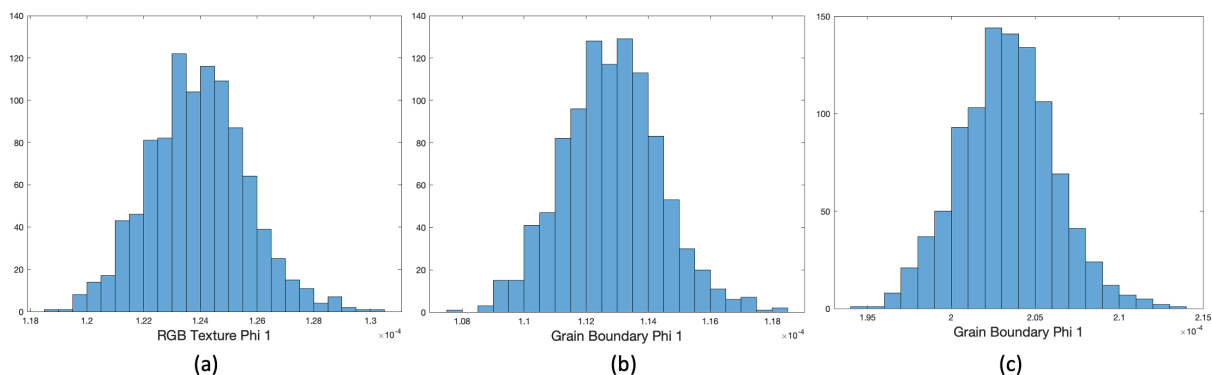


Figure 4.11: Histogram of the first Hu moment for 1000 normally distributed samples where (a) is $\phi_1$ of the original microstructure, (b) is $\phi_1$ of the neighbor analysis grain boundary network, and (c) is $\phi_1$ of the Euclidean distance grain boundary network.

Once the Hu moment distribution was made, these values were used as input for the artificial neural networks to examine the uncertainty propagation. Since it was determined in the conventionally forged case that the grain boundary inclusive artificial neural networks

consistently outperformed the no grain boundary method, only the grain boundary inclusive methods were analyzed. When looking at the distributions of $E_{11}$ in Fig. 4.12, the range of
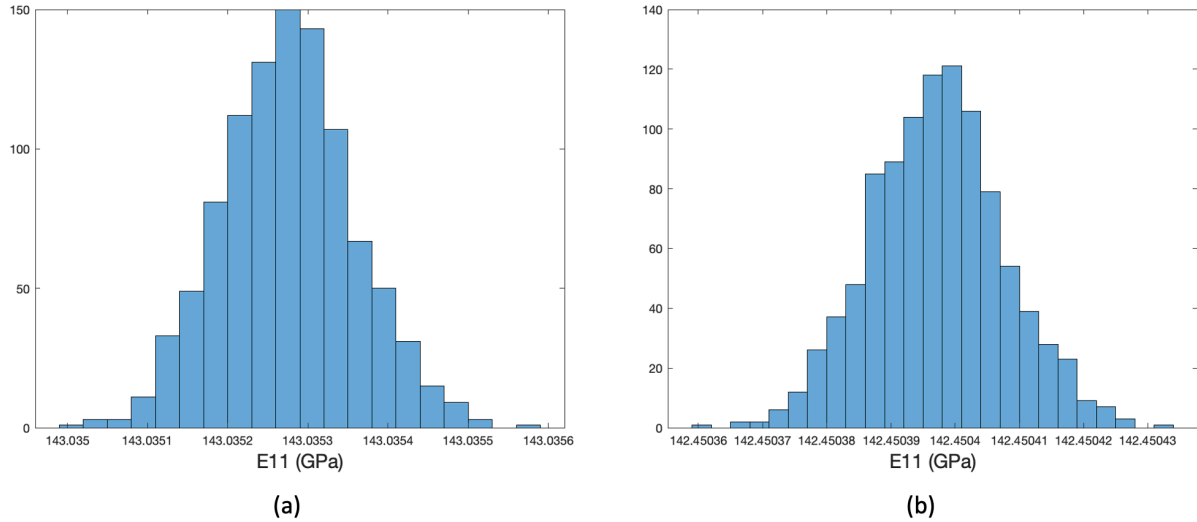


Figure 4.12: Histogram of $E_{11}$ obtained from the normally distributed Hu moments of LENS-produced samples where (a) is for neighbor analysis method and (b) is for Euclidean distance method.

As seen in Fig. 4.13, the results of $E_{22}$ are similarly very small. This could likely be because the Young's modulus value is not very sensitive for the microstructures examined.
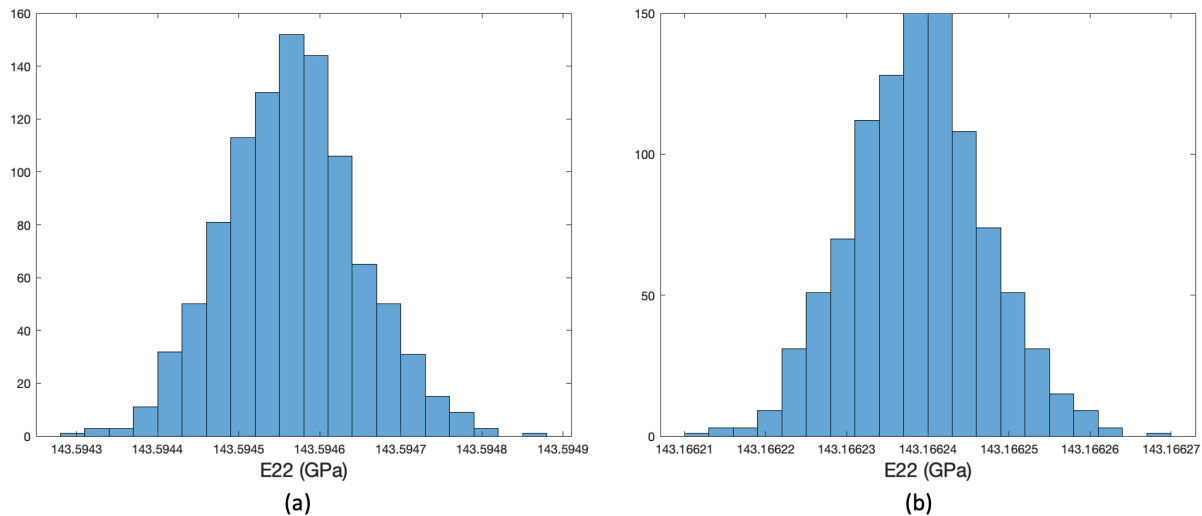


Figure 4.13: Histogram of $E_{22}$ obtained from the normally distributed Hu moments of LENS-produced samples where (a) is for neighbor analysis method and (b) is for Euclidean distance method.

Interestingly, this trend extends to the range of the predicted $\sigma_y$ values, as seen in Fig. 4.14. The small range of predicted values is unlike the range seen in the uncertainty propagation of the conventionally forged sample.
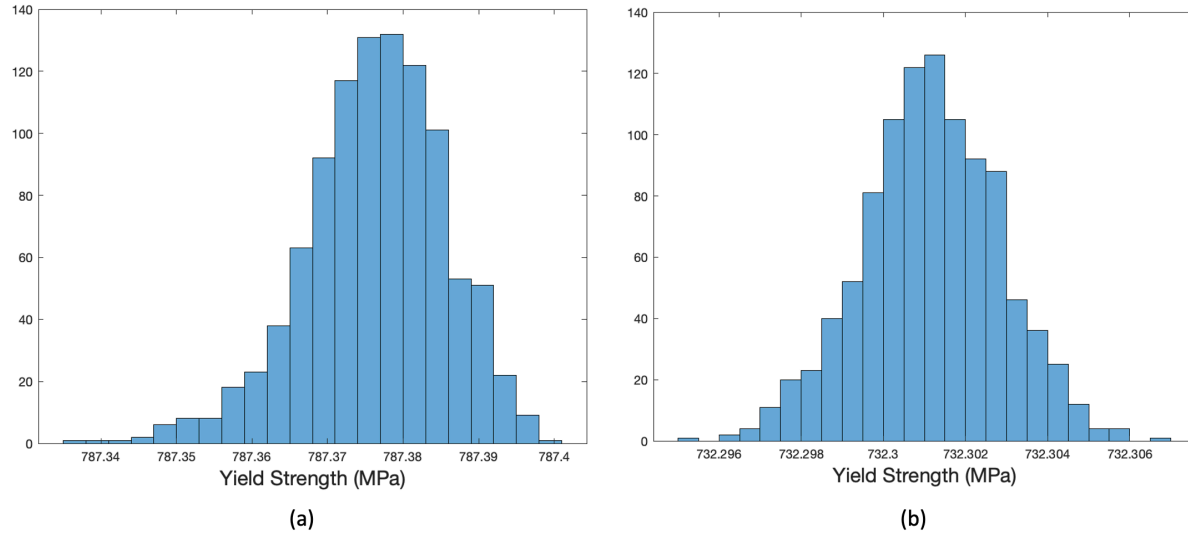


Figure 4.14: Histogram of $\sigma_y$ obtained from the normally distributed Hu moments of LENS-produced samples where (a) is for neighbor analysis method and (b) is for Euclidean distance method.

Though the range is unusual, the presence of a skewed distribution for the $\sigma_y$ predictions is consistent with the conventionally forged case. Overall, the trends of the prediction distributions for the LENS-produced case are consistent with those of the conventionally forged case, despite the smaller range of predicted values in the distributions. The conventionally forged samples show a higher uncertainty likely because they involved a higher number of grains, thus making impact of the grain boundaries more important than the LENS-produced samples.

# Chapter 5

# Conclusions

This work has covered a new strategy for material property prediction. Hu moments were applied to EBSD image data of microstructures in order to quantify them based on their pixel intensity values. This offers a benefit of reducing the memory needed for each sample because a quantified image data requires approximately 1000-times less memory than conventional image data, grains were separated based on their crystallographic orientation using k-means segmentation. This helped obtain volume fractions which could then be used for ODF, a method used for predicting homogenized properties of microstructures. For the grains of the same orientation, an additional step was implemented to separate individual grains. This technique can help when investigating the impact of grain shape on material properties. Grain boundaries have been shown to have a significant impact on the behavior of a microstructure. In order to evaluate this effect, two grain boundary identification methods were devised to show the network of the grain boundary. Once identified, the grain boundary was quantified with Hu moments and included as additional input to train an artificial neural network capable of predicting the Young's modulus and yield stress of the microstructure. It was shown that the grain boundary inclusive methods outperformed the method that did not include the grain boundary for all predicted properties in both conventionally forged and LENS-produced samples. After testing both the conventionally forged and LENS-produced cases, the Euclidean distance grain boundary method was found to outperform the tolerance-based neighbor analysis method. This could be due to the noise

reduction implemented by a less-strict approach to separating the grain boundary. Sensitivity analysis was conducted to determine the driving variable for material property prediction. Consistent with previous research, the first Hu moment was found to have the most significant impact on the result of the material property prediction. Uncertainty analysis was also conducted for both the conventionally forged and LENS-produced samples to determine the expected range of material properties that would come from uncertainty associated with the fabrication process. The conventionally forged case had a higher range of uncertainty likely due to the higher number of grains obtained.

Future work based on this work would involve:

- Expansion to three-dimensional samples - To do this, a cross-sectional approach could be employed using the same methodology. The three-dimensional analysis would need to be conducted in multiple axis directions in order to gauge the continuity of grains and grain boundaries as they exist in the sample.

- Investigation of more complex features that result from the fabrication process - Microstructural features that arise mainly from additive manufacturing include microtextures and melt pools. These are difficult to model and vary from sample to sample, even when using the same processing parameters.

- Evaluation of microstructure topology for other material classes (e.g. polymers, composites) for various applications - the major benefit of this work's approach being the reduction of computational expense.

# Chapter 6

# Summary

This work has developed numerical techniques to quantify microstructures using their image data. It is a useful strategy for reducing the computational expense of interpreting microstructure data. Furthermore it has been shown that the grain boundaries impact the homogenized material properties through a data-driven model based on artificial neural networks. Of the two methods of grain boundary identification, the Euclidean distance technique was shown to outperform the tolerance-based neighbor analysis, especially for the more complex additively manufactured samples. This grain boundary inclusive approach to predicting material properties can be used to examine more complex effects such as microtexture and melt pool cases. Furthermore, this work can be extended to evaluate three-dimensional cases using a cross-section approach, provided it is done in several axial directions in order to ensure continuity of grains and grain boundaries throughout the sample.

# Bibliography

[1] Blakey-Milner, B., et al. "Metal Additive Manufacturing in aerospace: A review", *Materials and Design*, Vol. 209, 110008, 2021.

[2] Gebler, M., A. Schoot-Uiterkamp, and C.Visser. "A global sustainability perspective on 3D printing technologies", *Energy Policy*, Vol. 74, 2014, pp: 158-167.

[3] Barz, A., T.Buer, and H.D.Haasis "A Study on the Effects of Additive Manufacturing on the Structure of Supply Networks", *IFAC-PapersOnLine*, Vol. 49, Issue 2, 2016, pp: 72-77.

[4] Allen, J. "An Investigation into the Comparative Costs of Additive Manufacture vs. Machine from Solid for Aero Engine Parts", *Cost Effective Manufacture via Net-Shape Processing*, 2006, pp: 17-1-17–10.

[5] Joshi, S.C., and A.A. Sheikh. "3D printing in aerospace and its long-term sustainability", *Virtual and Physical Prototyping*, Vol. 10, Issue 4, 2015, pp. 175-185.

[6] Campbell, T.A., Ivanova, O.S. "Additive Manufacturing as a Disruptive Technology: Implications of 3D Printing ", *Technology and Innovation*, Vol. 15, No. 1, 2013, pp. 67-79.

[7] SAE International, AS9100 - Quality Systems - Aerospace - Model for Quality Assurance in Design, Development, Production, Installation and Servicing, 1999.

[8] ISO/ASTM, Additive Manufacturing — Qualification principles (ISO/ASTM 52942-20), 2020.

[9] Lewandowski, J.J., and M. Seifi "Metal Additive Manufactruing: A Review of Mechanical Properties", *Annual Review of Materials Research*, Vol. 46, 2016, pp: 151-186.

[10] Seifi, M., et al. "Progress towards metal additive manufactruing standardization to support qualification and certification", *JOM*, Vol. 68, 2017, pp: 439-455.

[11] Attard, B., S.Cruchley, Ch.Beetz, M. Megahed, Y.L.Chiu, and M.M. Attallah. "Microstructural control during laser powder fusion to create graded microstructure Ni-superalloy components", *Additive Manufacturing*, Vol. 36, 2020, 101432.

[12] Collins, P.C., D.A. Brice, P. Samimi, I. Ghamarian, and H.L. Fraser. "Microstructural Control of Additive Manufacturing Metallic Materials", *Annual Review of Materials Research*, Vol. 46, 2016, pp: 63-91.

[13] Griffith, M. L., M.T. Ensz, J.D. Puskar, C.V. Robino, J.A. Brooks, J.A. Philliber, J.E. Smugeresky, and W.H. Hofmeister "Understanding the Microstructure and Properties of Components Fabricated by Laser Engineered Net Shaping", *Cambridge University Press*, Vol. 625, 2011.

[14] Griffith, M. L., M.T. Ensz, J.D. Puskar, C.V. Robino, J.A. Brooks, J.A. Philliber, J.E. Smugeresky, and W.H. Hofmeister. "Understanding the Microstructure and Properties of Components Fabricated by Laser Engineered Net Shaping", *Cambridge University Press*, Vol. 625, 2011.

[15] Attard, B., A.E-M.A. Mohamed, and M.M. Attallah. "Fundamentals of Laser Powder Bed Fusion of Metals", *Additively-Manufactured Materials and Technologies*, 2021, pp: 529-562.

[16] Miodownik, M.A. "A review of microstructural computer models used to simulate

grain growth and recrystallisation in aluminium alloys", *Journal of Light Metals*, Vol. 2, Issue 3, 2002, pp: 125-135.

[17] Song, Y., Z.X. Guo, and R.Yang. "First principles studies of TiAl-based alloys", *Journal of Light Metals*, Vol. 2, Issue 3, 2002, pp: 115-123.

[18] Senthilnathan, A. and P. Acar. "Multi-Scale Modeling for Texture and Grain Topology of Polycrystalline Microstructures under Uncertainty", *AIAA 2022-2106*, Session: Verification, Validation, and Uncertainty Quantification II, 2021.

[19] Kumar, M., W.E. King, and A.J.Schwartz. "Modifications to the microstructural topology in f.c.c. materials through thermomechanical processing", *Acta Materialia*, Vol. 48, Issue 9, 2000, pp: 2081-2091

[20] Dawson, P.R., S.R. MacEwen, and P-D. Wu. "Advances in sheet metal forming analyses: dealing with mechanical anisotropy from crystallographic texture", *International Materials Reviews*, Vol. 48, Issue 2, 2003, pp: 86-122.

[21] Li, W., R. Rezakhani, C. Jin, X. Zhou, and G. Cusatis. "A multiscale framework for the simulation of the anisotropic mechanical behavior of shale", *Numerical and Analytical Methods in Geomechanics*, Vol. 41, Issue 14, 2017, pp: 1494-1522.

[22] Falco, S., N. Fogell, S. Kasinos, and L. Iannucci. "Homogenisation of micromechanical modelling results for the evaluation of macroscopic material properties of brittle ceramics", *International Journal of Mechanical Sciences*, Vol. 220, 2022, 107071.

[23] Zhao, D., K. Matheson, B. Phung, S. Petruzza, M. Czabaj, and A. Spear. "Investigating the effect of grain structure on compressive response of open-cell metal foam using high-fidelity crystal-plasticity modeling", *Materials Science and Engineering: A*, Vol. 812, 2021, 140847.

[24] Wang, Q., J-S. Lecomte, C. Schuman, and A. Mandrelli. "The mechanical property evolution and grain boundary accommodation during hydride transformation in commercial pure titanium", *Materials Science and Engineering: A*, Vol. 812, 2021, 141099.

[25] Zhao, Z., R. Radovitzky, and A. Cuitiño. "A study of surface roughening in fcc metals using direct numerical simulation", *Acta Materialia*, Vol. 52, Issue 20, 2004, pp: 5791-5804.

[26] Pal, D., N. Patil, K. Zeng, and B. Stucker "An Integrated Approach to Additive manufacturing Simulations Using Physics Based, Coupled Multiscale Process Modeling", *Journal of Manufacturing Science and Engineering*, Vol. 136, Issue 6, 2014.

[27] Schwarzer, R.A., et al. "Electron Backscatter Diffraction in Material Science", *Springer*, 2009, pp: 1-20.

[28] Wright, S. I. and Nowell, M. M., "EBSD image quality mapping," *Microscopy and microanalysis*, Vol. 12, No. 1, 2006, pp: 72-84.

[29] Wright, S. I, "Fundamentals of automated EBSD", *Electron backscatter diffraction in materials science*, 1st ed., Vol. 2, Springer, Boston, MA, 2000, pp. 51-64.

[30] Schwartz, A.J., Kumar, M., Adams, B.L. and Field, D.P. eds., *Electron backscatter diffraction in materials science*, Vol. 2, Springer, New York, 2009, p. 403.

[31] Adams, B. L., S. I. Wright, and Karsten Kunze, "Orientation imaging: the emergence of a new microscopy," *Metallurgical Transactions A*, Vol. 24, No. 4, 1993, pp: 819-831.

[32] Dingley, D. J., and V. Randle, "Microtexture determination by electron back-scatter diffraction," *Journal of materials science*, Vol. 27, No. 17, 1992, pp: 4545-4566.

[33] Humphreys, F. J., "Characterisation of fine-scale microstructures by electron backscatter diffraction (EBSD)," *Scripta materialia*, Vol. 51, No. 8, 2004, pp: 771-776.

[34] Rathmayr, G.B., A. Hohenwarter, and R. Pippan. "Influence of grain shape and orientation on the mechanical properties of high pressure torsion deformed nickel", *Materials Science and Engineering*, Vol. 560, 2013, pp: 224-231.

[35] Simonelli, M., Y.Y. Tse, and C. Tuck. "Effect of the build orientation on the mechanical properties and fracture modes of SLM Ti–6Al–4V", *Materials Science and Engineering*, Vol. 616, 2014, pp: 1-11.

[36] Watanabe, T. "Grain boundary engineering: historical perspective and future prospects", *Journal of Material Science*, Vol. 46, 2011, pp: 4095-4115.

[37] Watanabe, T., M. Yamada, and S. Karashima. "Grain boundary strengthening associated with $\Sigma = 9$ near-coincidence boundary in 1010 twist zinc bicrystals at high temperatures", *Philosophical Magazine*, Vol. 63, Issue 5, 1991, pp: 1013-1022.

[38] Yoshida, H., et al. "A change in the chemical bonding strength and high-temperature creep resistance in Al2O3 with lanthanoid oxide doping", *Philosophical Magazine*, Vol. 82, Issue 3, 2002, pp: 511-525.

[39] Hu, M., "Visual pattern recognition by moment invariants," *IRE transactions on information theory*, Vol. 8, No. 2, pp: 179-187, 1962.

[40] Catania, R., A. Senthilnathan, J. Sions, K. Snyder, H. Al-Ghaib, B. Zimmerman, and P. Acar. "New Methodologies for Grain Boundary Detection in EBSD Data of Microstructures", AIAA 2022-1424 Session: Materials and Design for Additive Manufacturing II, 2021.

[41] Acar, P., and V. Sundararaghavan. "Utilization of a Linear Solver for Multiscale Design and Optimization of Microstructures", *AIAA Journal*, Vol. 54, No. 5, 2016, pp: 1751-1759.

[42] Javaheri, I., and V. Sundararaghavan, "Polycrystalline Microstructure Reconstruction Using Markov Random Fields and Histogram Matching," *Computer-Aided Design*, 120, (2020) 102806.

[43] Acar, P. "Crystal Plasticity Model Calibration for Ti-7Al Alloy with a Multi-fidelity Computational Scheme," *Integrating Materials and Manufacturing Innovation*, Vol. 7, pp: 186–194, 2018.

[44] Sundararaghavan, V., and N. Zabaras, "Classification and reconstruction of three-dimensional microstructures using support vector machines", *Computational Materials Science*, Vol. 32, No. 2, 2005, pp: 223-239.

[45] MacSleyne, J. P. "Moment invariants for 2-D and 3-D characterization of the morphology of gamme-prime precipitates in nickel-base superalloys," Ph.D. Dissertation, Carnegie Mellon University, Pittsburgh, PA, 2008.

[46] Sahir, S., "Canny Edge Detection Step by Step in Python — Computer Vision," *toward data science*, January 25, 2019.

[47] MacSleyne, J. P., J. P. Simmons, and M. DeGraef, "On the use of 2-D moment invariants for the automated classification of particle shapes," *Acta Materialia*, Vol. 56, No. 3, 2008, pp: 427-437.

[48] Foresee, D.F., and M. T. Hagan. "Gauss-Newton approximation to Bayesian learning." *Proceedings of the International Joint Conference on Neural Networks*, June, 1997.

[49] Senthilnathan, A., and P. Acar, and Marc De Graef. "Markov Random Field based microstructure reconstruction using the principal image moments." *Materials Characterization* Vol. 178, 2021: 111281.

[50] Senthilnathan, A., and P. Acar. "Shape Moment Invariants as a New Methodology for Uncertainty Quantification in Microstructures." AIAA Scitech 2021 Forum. 2021.

[51] Acar, P., and V. Sundararaghavan. "Uncertainty Quantification of Microstructural Properties due to Experimental Variations", AIAA Journal, Vol. 55, No: 8, 2017, pp: 2824-2832.

[52] Yaghoobi, M., S. Ganesan, S. Sundar, A. Lakshmanan, S. Rudraraju, J.E. Allison, and V. Sundararaghavan. PRISMS-Plasticity: An open-source crystal plasticity finite element software, Computational Materials Science, 169, 109078 (2019).

[53] Anand L and Kothari MA (1996) Computational procedure for rate-independent crystal plasticity, J. Mech. Phys. Solids, 44: 525–558.

[54] Sha W and Malinov S (2009) Titanium Alloys: Modelling of Microstructure, Properties and Applications, Elsevier, Amsterdam, The Netherlands.

[55] Nervo L, King A, Fitzner A, Ludwig W and Preuss M (2016) A study of deformation twinning in a titanium alloy by X-ray diffraction contrast tomography, Acta Materialia, 105: 417–428.

[56] Balasubramanian, S (1998) Application to Deformation Processing of Lightweight Metals. Ph.D. Dissertation, Massachusetts Institute of Technology, Cambridge, MA, USA.

[57] Williams JC, Baggerly RG and Paton NE (2002) Deformation Behavior of HCP Ti-Al Alloy Single Crystals, Metall. Mater. Trans. A, 33, 837.

[58] Lutjering G and Williams J (2007) Introduction. In Titanium, 2nd ed.; Springer: Berlin, Germany.

[59] Lienert U, Brandes MC, Bernier JV, Weiss J, Shastri SV, Mills MJ and Miller MP (2009) In-situ single-grain peak profile measurements on Ti-7 Al during tensile deformation, Mater. Sci. Eng. A, 524: 46–54.

[60] Khan AS, Kazmia R, Farrokha B and Zupana M (2007) Effect of oxygen content and microstructure on the thermo-mechanical response of three Ti-6Al-4V alloys: Experiments and modeling over a wide range of strain-rates and temperatures. Int. J. Plast., 23: 1105–1125.

[61] Fitzner AG (2014) Effects of Alloying Elements on Twinning in alpha-Titanium Alloys. Ph.D. Dissertation, University of Manchester, Manchester, UK, p. 261.

[62] Fitzner AG, Prakash DGL, Fonseca JQ, Thomas M, Zhang S, Kelleher J, Manuel P and Preuss M (2016) The effect of aluminum on twinning in binary alpha-Titanium, Acta Materialia, 103: 341–351.

[63] Acar P (2018) Crystal Plasticity Model Calibration for Ti-7Al Alloy with a Multi-Fidelity Computational Scheme, Integrating Materials and Manufacturing Innovation, Vol. 7, No. 4, pp: 186-194.

[64] Acar P and Sundararaghavan V (2017) Uncertainty Quantification of Microstructural Properties due to Variability in Measured Pole Figures, Acta Materialia,124: 100–108.

# Appendices

# Appendix A

# Crystal Plasticity Modeling using PRISMS

## A.1  Crystal Plasticity Modeling

For crystal plasticity modeling, the rate-independent single crystal plasticity constitutive model developed by Anand and Kothari [53] is used to compute the macroscopic stress of the polycrystalline material. The parameters of interest in this work are the slip system parameters, and the used slip system hardening model is given below:

$$h^{\alpha\beta} = [q + (1-q)\delta^{\alpha\beta}]h^{\beta} \quad \text{(no sum on } \beta) \tag{A.1}$$

where $h^{\beta}$ is a single slip hardening rate, $q$ is the latent-hardening ratio and $\delta^{\alpha\beta}$ is the Kronecker delta function. The parameter $q$ is taken to be 1.0 for coplanar slip systems and 1.4 for non-coplanar slip systems. For the single-slip hardening rate, the following specific form is adopted:

$$h^{\beta} = h_o(1 - \frac{s^{\beta}}{s_s})^a \tag{A.2}$$

where $h_o$, $a$, and $s_s$ are slip hardening parameters. The basal $< a >$, prismatic $< a >$,

pyramidal $< a >$ and pyramidal $< c + a >$ slip systems, and $10\bar{1}2 < \bar{1}011 >$ twinning mechanism are computationally modeled. The elastic parameters of Ti-7Al are taken as [54]: $C_{11} = C_{12} = 175$ GPa, $C_{33} = 220$ GPa, $C_{12} = 88.7$ GPa, $C_{13} = C_{23} = 62.3$ GPa, $C_{44} = C_{55} = 62.2$ GPa, and $C_{66} = (C_{11} - C_{12})/2$.

The Ti-7Al alloy has an hexagonal close-packed (HCP) crystallographic structure. The crystal plasticity simulation modeled the microstructure using 750 grain and $32 \times 32 \times 32$ elements. The grain orientations in the crystal plasticity simulation is assigned to match with the texture of the experimental data.

The HCP metals are known to exhibit an easy $< a >$ slip, either on the prismatic or basal plane [55]. The slip systems of the Ti-7Al are determined as the three equivalent basal $0001 < 11\bar{2}0 >$, three equivalent prismatic $10\bar{1}0 < 11\bar{2}0 >$ and six equivalent pyramidal $10\bar{1}1 < 11\bar{2}0 >$ slip systems [56]. All these three slip systems share a common slip direction, $< 11\bar{2}0 >$, or $< a >$. The slip on the basal, prismatic and pyramidal slip systems is denoted as $< a >$-slip. Additional slip or twin mechanisms are required to accommodate a strain parallel to the $c$-axis of the hexagonal system. One mode slips on pyramidal planes with $< 11\bar{2}3 >$, or $< c + a >$ slip directions [56]. Moreover, the recent studies in the literature [55, 56, 57, 58, 59, 60, 61, 62] revealed the existence of the $10\bar{1}2 < \bar{1}011 >$ tensile twin, which provides an approximately 90 degrees rotation of the $c$-axis from a tensile stress to the compressive stress condition and increases the basal texture intensity during compressive loading. The slip and twin system parameters calibrated recently for the crystal plasticity modeling of Ti-7Al alloy are used in the present work [63].

## A.2   Experimental Data for Forged Ti-7Al Alloy

The description for the used experimental data is given as follows [64]. The sample Ti-7Al alloy has a beta transus temperature of $1050^{o}$C. The alloy was forged from a 7.5 inch round

ingot to a 4 inch square ingot at 1142$^o$C and air cooled. Three different cylindrical samples 6 mm in diameter and 9 mm in height were machined from the forged ingot. The samples were then subject to the same process: compression to a 20% height reduction at a strain rate of 0.03 mm/min at room temperature followed by annealing in a tube furnace at 800$^o$C for 72 hours followed by a water quench. The samples were sectioned perpendicular to the compression axis, mounted in epoxy and polished to a final step of colloidal silica. The measured texture was found to be close to the randomly oriented texture.